Production of HONO from heterogeneous uptake of NO₂ on illuminated TiO₂ aerosols measured by Photo-Fragmentation Laser Induced Fluorescence

Joanna E. Dyson[1], Graham A. Boustead[1], Lauren T. Fleming[1], Mark Blitz[1, 2], Daniel Stone[1],
Stephen R. Arnold[3], Lisa K. Whalley[1, 2], Dwayne E. Heard[1]*

[1] *School of Chemistry, University of Leeds, LS2 9JT, UK.*

[2] *National Centre of Atmospheric Science, University of Leeds, LS2 9JT, UK.*

[3] *School of Earth and Environment, University of Leeds, LS2 9JT, UK.*

Corresponding Author. Email: D.E.Heard@leeds.ac.uk

Abstract

The rate of production of HONO from illuminated TiO₂ aerosols in the presence of NO₂ was measured using an aerosol flow tube coupled to a photo-fragmentation laser induced fluorescence detection apparatus. The reactive uptake coefficient of NO₂ to form HONO, $\gamma_{NO_2 \rightarrow HONO}$, was determined for NO₂ mixing ratios in the range $34 - 400$ ppb, with $\gamma_{NO_2 \rightarrow HONO}$ spanning the range $(9.97 \pm 3.52) \times 10^{-6}$ to $(1.26 \pm 0.17) \times 10^{-4}$ at a relative humidity of 15 ± 1 % and for a lamp photon flux of $(1.63 \pm 0.09) \times 10^{16}$ photons cm^{-2} s^{-1} (integrated between 290 and 400 nm), which is similar to values of ambient actinic flux at midday. $\gamma_{NO_2 \rightarrow HONO}$ increased as a function of NO₂ mixing ratio at low NO₂ before peaking at $(1.26 \pm 0.17) \times 10^{-4}$ at 51 ppb NO₂ and then sharply decreasing at higher NO₂ mixing ratios, rather than levelling off which would be indicative of surface saturation. The dependence of HONO production on relative humidity was also investigated, with a peak in production of HONO from TiO₂ aerosol surfaces found at ~25 % RH. Possible mechanisms consistent with the observed trends in both the HONO production and reactive uptake coefficient were investigated using a zero-dimensional kinetic box model. The modelling studies supported a mechanism for HONO production on the aerosol surface involving two molecules of NO₂, as well as a surface HONO loss mechanism which is dependent upon NO₂. In a separate experiment, significant production of HONO was observed from illumination of mixed nitrate/TiO₂ aerosols in the absence of NO₂. However, no statistically significant production of HONO was seen from the illumination

30   of pure nitrate aerosols. The rate of production of HONO observed from mixed nitrate/TiO_2

31   aerosols was scaled to ambient conditions found at the Cape Verde Atmospheric Observatory

32   (CVAO) in the remote tropical marine boundary layer. The rate of HONO production from

33   aerosol particulate nitrate photolysis containing a photocatalyst was found to be similar to the

34   missing HONO production rate necessary to reproduce observed concentrations of HONO at

35   CVAO. These results provide evidence that particulate nitrate photolysis may have a significant

36   impact on the production of HONO and hence NO_x in the marine boundary layer where mixed

37   aerosols containing nitrate and a photocatalytic species such as TiO_2, as found in dust, are

38   present.

39

40   **1   Introduction**

41   A dominant source of OH radicals in polluted environments is the photolysis of nitrous acid

42   (HONO) (Platt et al., 1980;Winer and Biermann, 1994;Harrison et al., 1996;Alicke et al.,

43   2002;Whalley et al., 2018;Crilley et al., 2019;Lu et al., 2019;Slater et al., 2020;Whalley et al.,

44   2020). During a recent study in Winter in central Beijing, HONO photolysis accounted for over

45   90 % of the primary production of OH averaged over the day (Slater et al., 2020). Oxidation

46   by OH radicals is the dominant removal mechanism for many tropospheric trace gases, such as

47   tropospheric methane, as well as the formation of secondary species, including tropospheric

48   ozone (Levy, 1971), nitric and sulphuric acids which condense to form aerosols, and secondary

49   organic aerosols. Understanding the formation of HONO in highly polluted environments is

50   crucial to fully understand both the concentration and distribution of key atmospheric radical

51   species, as well as secondary products in the gas and aerosol phases associated with climate

52   change and poor air quality.

53   Atmospheric concentrations of HONO range from a few pptv in remote clean environments

54   (Reed et al., 2017) to more than 10 ppb in highly polluted areas such as Beijing (Crilley et al.,

55   2019). The main gas-phase source of HONO in the troposphere is the reaction of nitric oxide

56   (NO) with the OH radical. HONO has also been shown to be directly emitted from vehicles

57   (Kurtenbach et al., 2001;Li et al., 2008), for which the rate of emission is often estimated as a

58   fraction of known NO_x (NO_2+NO) emissions. Many heterogeneous HONO sources have also

59   been postulated including the conversion of nitric acid (HNO_3) on ground or canopy surfaces

60   (Zhou et al., 2003;George et al., 2005), bacterial production of nitrite on soil surfaces (Su et

61   al., 2011;Oswald et al., 2013) and, more recently, particulate nitrate photolysis, thought to be

62 an important source in marine environments (Ye et al., 2016;Reed et al., 2017;Ye et al.,

63 2017a;Ye et al., 2017b). Rapid cycling of gas-phase nitric acid to gas-phase nitrous acid via

64 particulate nitrate photolysis in the clean marine boundary layer has been observed during the

65 2013 NOMADSS aircraft measurements campaign over the North Atlantic Ocean (Ye et al.,

66 2016). Ground-based measurements of HONO made at Cape Verde in the tropical Atlantic

67 Ocean (Reed et al., 2017) provided evidence that a mechanism for renoxification in low NO_x

68 areas is required (Reed et al., 2017;Ye et al., 2017a).

69 Recent model calculations show a missing daytime source of HONO, which is not consistent

70 with known gas-phase production mechanisms, direct emissions or dark heterogeneous

71 formation (e.g. prevalent at night). It has been suggested that this source could be light driven

72 and dependent on NO_2 (Kleffmann, 2007;Michoud et al., 2014;Spataro and Ianniello, 2014;Lee

73 et al., 2016).

74 It is estimated that between 1604 and 1960 Tg yr^{-1} of dust particles are emitted into the

75 atmosphere (Ginoux et al., 2001). Titanium dioxide (TiO_2) is a photocatalytic compound found

76 in dust particles at mass mixing ratios of between 0.1 and 10 % depending on the location the

77 particles were suspended (Hanisch and Crowley, 2003). When exposed to UV light ($\lambda < 390$

78 nm) TiO_2 promotes an electron (e_{CB}^-) from the conduction band to the valence band leaving

79 behind a positively charged hole (h_{VB}^+) in the valence band (Chen et al., 2012):

$$TiO_2 + h\nu \rightarrow e_{CB}^- + h_{VB}^+ \tag{R1}$$

80 which can then lead to both reduction and oxidation reactions of any surface adsorbed gas-

81 phase species such as NO_2 leading to HONO.

82 In previous studies of the reaction of NO_2 on TiO_2 aerosol surfaces, HONO was observed as a

83 major gas-phase product (Gustafsson et al., 2006;Dupart et al., 2014). Gustafsson *et al.*, (2006)

84 observed a yield of gas-phase HONO of ~ 75 % (for each NO_2 removed), and showed the rate

85 of the photoreaction of NO_2 on pure TiO_2 aerosols depended on relative humidity, emphasising

86 the superhydrophilic nature of TiO_2 surfaces under UV irradiation. Dupart *et al.* (2014) also

87 reported a relative humidity dependence of the uptake of NO_2 onto Arizona Test Dust

88 containing TiO_2 with the main gas-phase products measured being NO and HONO, with a

89 HONO yield of 30 % in experiments with 110 ppb NO_2. Dupart et al. (2014) postulated the

90 following mechanism of HONO production, which is consistent with the formation of the NO_2^-

91 anion seen in a previous study on TiO_2 surfaces (Nakamura et al., 2000):

$$h_{VB}^+ + H_2O \rightarrow H^+ + OH \tag{R2}$$

$$e_{CB}^- + O_2 \rightarrow O_2^- \tag{R3}$$

$$NO_2 + O_2^- (or\ e_{CB}^-) \rightarrow NO_2^- + O_2 \tag{R4}$$

$$NO_2^- + H^+ \rightarrow HONO \tag{R5}$$

$$NO_2 + OH \rightarrow HNO_3 \tag{R6}$$

92 In areas with high mineral dust loading, such as desert regions, far from anthropogenic sources,
93 NO_2 concentrations are typically low. However, when dust is transported to urban areas, this
94 source of HONO may become significant. One study reported that TiO_2 composed 0.75-1.58
95 µg m^{-3} when aerosol loadings were 250-520 µg m^{-3} over the same time period in southeast
96 Beijing, when air had been transported from the Gobi desert (Schleicher et al., 2010).

97 In this study, the production of HONO on the surface of TiO_2 particles in the presence of NO_2
98 is investigated as a function of NO_2 mixing ratio, aerosol surface area density and relative
99 humidity using an aerosol flow tube system coupled to a photo-fragmentation laser induced
100 fluorescence detector (Boustead, 2019). The uptake coefficient of NO_2 to generate HONO is
101 then determined, and a mechanistic interpretation of the experimental observations is
102 presented. The production of HONO directly in the absence of NO_2 from the illumination of a
103 mixed sample of nitrate and TiO_2 aerosol is also presented. Using a similar apparatus, previous
104 work had showed that TiO_2 particles produce OH and HO_2 radicals directly under UV
105 illumination (Moon et al., 2019). The atmospheric implications of these results and the role of
106 photo-catalysts for the formation of HONO are also discussed.

107 **2   Method**

108 **2.1   Overview of the Experimental Setup**

109 The production of HONO from illuminated aerosol surfaces is studied using an aerosol flow
110 tube system coupled to a photo-fragmentation laser induced fluorescence (PF-LIF) cell which
111 allows the highly sensitive detection of the OH radical formed through photo-fragmentation of
112 HONO into OH and NO followed by Laser-Induced Fluorescence (LIF) detection at low
113 pressure. The experimental setup used in this investigation is described in detail in (Boustead,
114 2019), therefore only a brief description of the setup is given here. A schematic of the
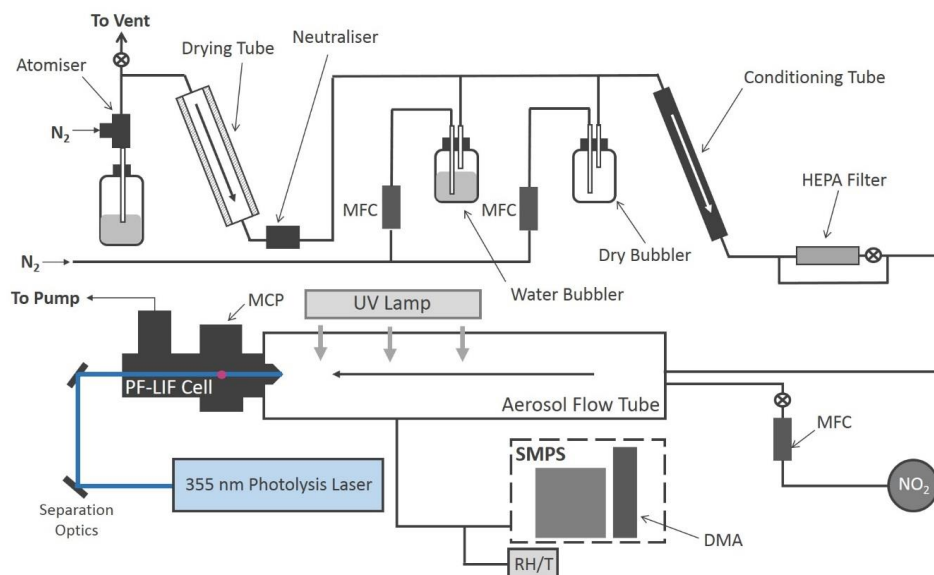115 experimental setup is shown in Figure 1.

Figure 1. Schematic of the Leeds aerosol flow tube system coupled to a laser-fragmentation laser-induced fluorescence detector for HONO. The paths of the 355 nm (blue) and 308 nm (purple, depicted as travelling out of the page perpendicular to the 355 nm light) light are also shown. CPC: condensation particle counter; DMA: differential mobility analyser; HEPA: high efficiency particle air filter; FAGE: fluorescence assay by gas expansion; MCP: microchannel plate photomultiplier; MFC: mass flow controller; RH/T: relative humidity/ temperature probe; SMPS: scanning mobility particle sizer.

116

117   All experiments were conducted at room temperature (295 ± 3 K) using nitrogen (BOC, 99.998

118   %) or air (BOC, 21 ± 0.5 % O_2) as the carrier gas. A humidified flow of aerosols, ~ 6 lpm (total

119   residence time of 104 s in the flow tube), was introduced through an inlet at the rear of the

120   aerosol flow tube (Quartz, 100 cm long, 5.75 cm ID) which was covered by a black box to

121   eliminate the presence of room light during experiments. A 15 W UV lamp (XX-15LW Bench

122   Lamp, λ_{peak}=365 nm) was situated on the outside of the flow tube to illuminate aerosols and

123   promote the production of HONO (half the length of the flow tube was illuminated leading to

124   an illumination time of 52 s). The concentration of HONO is measured by PF-LIF with

125   sampling from the end of the flow tube via a protruding turret containing a 1 mm diameter

126   pinhole, through which the gas exiting the flow tube was drawn into the detection cell at 5 lpm.

127   The detection cell was kept at low pressure, ~ 1.5 Torr, using a rotary pump (Edwards, E1M80)

128   in combination with a roots blower (Edwards, EH1200). All gas flows in the experiment were

129   controlled using mass flow controllers (MKS and Brooks). The relative humidity (RH) and

130   temperature of the aerosol flow was measured using a probe (Rotronics HC2-S, accuracy ±1

131   % RH) the former calibrated against the H_2O vapour concentration measured by a chilled

132   mirror hygrometer (General Eastern Optica), in the exhaust from the flow tube.

2.2   Aerosol generation and detection

134   Solutions for the generation of TiO_2 aerosol solutions were prepared by dissolving 5 g of

135   titanium dioxide (Aldrich Chemistry 718467, 99.5% Degussa, 80 % anatase: 20 % rutile) into

136   500 ml of milli-Q water. Polydisperse aerosols were then generated from this solution using an

137   atomiser (TSI model 3076) creating a 1 lpm flow of TiO_2 aerosol particles in nitrogen hereafter

138   referred to as the aerosol flow. This aerosol flow was then passed through a silica drying tube

139   (TSI 3062, capable of reducing 60 % RH incoming flow to 20 % RH) to remove water vapour,

140   then passed through a neutraliser to apply a known charge distribution and reduce loss of

141   aerosols to the walls. After the neutraliser the aerosol flow was mixed with both a dry and a

142   humidified N_2 flow (controlled by MFCs) to regulate the relative humidity of the system by

143   changing the ratio of dry to humid nitrogen flows. A conditioning tube was then used to allow

144   for equilibration of water vapour adsorption and re-evaporation to and from the aerosol surfaces

145   for the chosen RH, which was controlled within the range ~10-70 % RH. A portion of the

146   aerosol flow was then passed through a high efficiency particle filter (HEPA) fitted with a

147   bypass loop and bellows valve allowing control of the aerosol number concentration entering

148   the aerosol flow tube. Previous studies (George et al., 2013;Boustead, 2019) have shown the

149   loss of aerosol to the walls of the flow tube to be negligible. Aerosol size distributions were

150   measured for aerosols exiting the flow tube using a scanning mobility particle sizer (SMPS,

151   TSI 3081) and a condensation particle counter (CPC, TSI 3775) which was calibrated using

152   latex beads. Any aerosol surface area not counted due to the upper diameter range of the

153   combined SMPS/CPC (14.6 – 661.2 nm, sheath flow of 3 lpm, instrumental particle counting

154   error of 10-20 %) was corrected for during analysis by assuming a lognormal distribution,

155   which was verified for TiO_2 aerosols generated in this manner (Matthews et al., 2014).

156   However, the majority of aerosols, >90 %, had diameters in the range that could be directly

157   detected. Previously, we had determined by imaging the aerosols using a scanning electron

158   microscope (SEM) that the particles were spherical (Moon et al., 2018). In addition to the

159   experiments with single-component TiO_2, mixed ammonium nitrate/TiO_2 and single-

160   component ammonium nitrate aerosols were also generated using the atomiser for

161   investigations of HONO production from nitrate aerosols without NO_2 present. An example of

162   an aerosol size distribution from this work for single-component ammonium nitrate aerosols,

163   mixed ammonium nitrate/TiO_2 and single-component TiO_2 aerosols is shown in Figure 2.
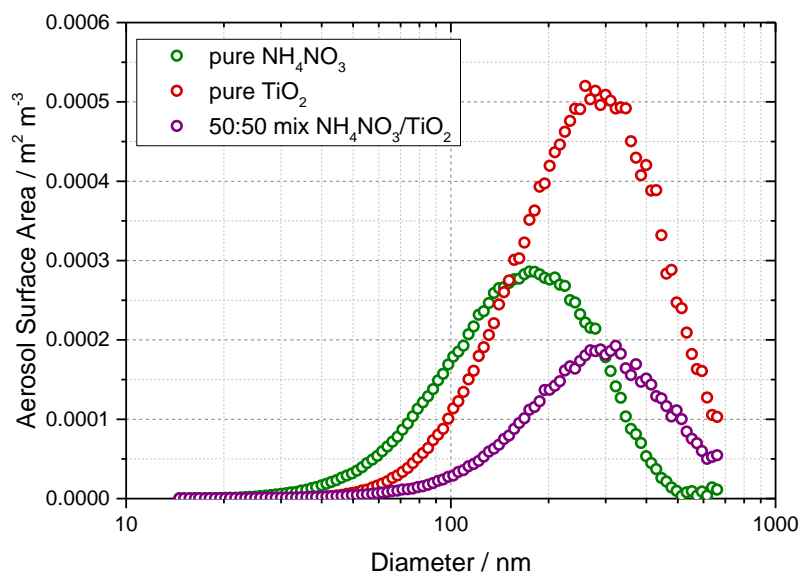
Figure 2 Typical aerosol surface area distribution for pure ammonium nitrate aerosols (green) and pure TiO_2 aerosols (red) and 50:50 mixed nitrate/TiO_2 aerosols (purple) measured after the flow tube.

2.3 Detection of HONO

164

165 As HONO is not directly detectable via LIF, it was necessary to fragment the HONO produced

166 into OH and NO (Liao et al., 2006), with detection of OH via LIF. A 355 nm photolysis laser

167 (Spectron Laser Systems, SL803) with a pulse repetition frequency (PRF) of 10 Hz and pulse

168 duration ~ 10 ns was used to fragment HONO into OH. This fragmentation wavelength was

169 chosen as HONO has a strong absorption peak at ~ 355 nm leading to the breakage of the HO-

170 NO bond to form NO and OH in their electronic ground states (Shan et al., 1989). A Nd:YAG

171 pumped dye probe laser (JDSU Q201-HD, Q-series, Sirah Cobra Stretch) with a PRF of 5000

172 Hz, was used for the detection of OH via the fluorescence assay by gas expansion (FAGE)

173 technique which employs the expansion of gas through a small pinhole into the detection cell.

174 The OH radical was measured using on-resonance detection by LIF via the excitation of the

175 $A^2\Sigma^+ (v' = 0) \leftarrow X^2\Pi_i (v'' = 0)$ Q$_1$(2) transition at 308 nm (Heard, 2006). A multi-channel plate

176 (MCP) photomultiplier (Photek, MCP 325) equipped with an interference filter at 308 nm (Barr

177 Associates, 308 nm. FWHM – 8 nm, ~50 % transmission) was used to measure the fluorescence

178 signal. A reference OH cell in which a large LIF signal could be generated was utilised to

Atmospheric
Chemistry
and Physics
Discussions
Open Access
EGU

179   ensure the wavelength of the probe laser remained tuned to the peak of the OH transition at

180   308 nm. OH measurements are taken both before and after each photolysis laser pulse allowing

181   measurement of any OH already present in the gas flow to be determined as a background

182   signal for subtraction. The OH generated from HONO photolysis was measured promptly

183   (~800 ns) after the 355 nm pulse to maximise sensitivity to OH before it was spatially diluted

184   away from the measurement region (Boustead, 2019). Offline measurements, with the probe

185   laser wavelength moved away from the OH transition (by 0.02 nm), were taken to allow the

186   signal generated from detector dark counts and scattered laser light to be measured and

187   subtracted from the online signal. To determine an absolute value of the HONO concentration,

188   [HONO], a calibration was performed, in order to convert from the HONO signal, S_{HONO}, using

189    $S_{HONO} = C_{HONO}$ [HONO], as described fully in (Boustead, 2019). A glass calibration wand was

190   used to produce OH and HO_2 in equal concentrations from the photolysis of water vapour at

191   185 nm:

$$H_2O + h\nu \xrightarrow{\lambda = 185\ nm} OH + H \qquad (R7)$$

$$H + O_2 + M \rightarrow HO_2 + M \qquad (R8)$$
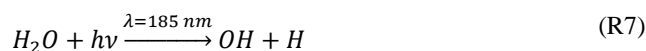
192   An excess flow of NO was then added to generate HONO which was then detected as OH in

193   the cell. The excess flow of NO (BOC, 99.5 %) ensures rapid and complete conversion of OH

194   and HO_2 to HONO. The concentration of OH and HO_2 produced, and therefore the amount of

195   HONO produced in the wand, is calculated using:

$$[OH] = [HO_2] = [H_2O]\ \sigma_{H2O}\ \phi_{OH}\ F\ t \qquad (1)$$

196   where [H_2O] is the concentration of water vapour in the humidified gas flow, σ_{H2O} is the

197   absorption cross section of H_2O at 185 nm (7.14×10^{-20} cm^2 molecule^{-1} (Cantrell et al., 1997),

198   ϕ_{OH} is the quantum yield of OH for the photo-dissociation of H_2O at 185 nm (=1), F is the

199   lamp flux and t is the irradiation time (the product of which is determined using ozone

200   actinometry (Boustead, 2019).

201   A typical value of the calibration factor was $C_{HONO} = (3.63 \pm 0.51) \times 10^{-9}$ counts mW^{-1} for N_2,

202   leading to a calculated limit of detection of 12 ppt for a 50 s averaging period and a signal-to-

203   noise ratio (SNR) of 1 (Boustead, 2019). The typical error in the HONO concentration was

204   15% at 1σ, determined by the error in the calibration.

2.4 Experimental procedure and data analysis

The experiments were performed with a minimum flow of 6 lpm through the aerosol flow tube giving a Reynolds number of ~ 150 which ensured a laminar flow regime. The HONO signal, converted to an absolute concentration using a calibration factor, was measured over a range of aerosol surface area densities, both in the presence and absence of illumination, and background measurements without aerosols present, were also performed.

The HONO signal originates from several sources: the illuminated aerosol surface; the illuminated quartz flow tube walls; dark reactions on aerosol surfaces; dark reactions on the flow tube surface and finally from impurities in the NO_2 (Sigma Aldrich, >99.5 %, freeze pump thawed to further remove any remaining NO or O_2) and N_2 flows (either HONO itself or a species which photolyses at 355 nm to give OH). Of interest here is the HONO production from both dark and illuminated aerosol surfaces which is atmospherically relevant. Following transit through the flow tube, and in the presence of NO_2, the total concentration of HONO measured by the PF-LIF detector is given by:

$$[HONO] = [HONO]_{illuminated\ aerosols} + [HONO]_{illuminated\ walls} \\ + [HONO]_{dark\ aerosols} + [HONO]_{dark\ walls} + [HONO]_{impurities}$$

(2)

Any HONO seen without the presence of aerosol was therefore due to HONO impurities in the N_2 or NO_2 gas, the dark production of HONO from the flow tube walls or from the production of HONO from the illuminated reactor walls, which may include production from TiO_2 aerosols coating the flow tube in the presence of NO_2. This background HONO concentration depended on the experimental conditions and on how recently the flow tube and PF-LIF cell had been cleaned to remove any build-up of TiO_2 deposits. However, the build-up of TiO_2 on the flow tube walls was relatively slow and back-to-back measurements were made in the presence and absence of aerosols to obtain an accurate background. Even though the aerosol surface area density (~0.02 m^2 m^{-3}) was small compared to the surface area density of the reactor walls (35 m^2 m^{-3}), very little HONO signal was produced without the presence of aerosols, and was always subtracted from the signal in the presence of aerosols. The HONO signal was measured both with the lamp on and off for each aerosol surface area density to investigate the production of HONO from illuminated aerosol surfaces. The HONO signal was averaged over 50 s (average of 500 of the 355 nm photolysis laser pulses with a PRF of 10 Hz). Once aerosols were introduced into the flow tube system a period of ~ 30 min was allowed for equilibration and the measured aerosol surface area density to stabilise. In general, the relative

235   humidity of the system was kept constant at RH ~ 15 % for all experiments investigating

236   HONO production as a function of NO_2 mixing ratio over the range 34 - 400 ppb. In a number

237   of experiments, however, RH was varied in the range ~12-37 %.

238   The mixing ratio of NO_2 entering the flow tube was calculated using the concentration of the

239   NO_2 in the cylinder and the degree of dilution. The NO_2 mixing ratio within the cylinder was

240   determined using a commercial instrument based on UV-Vis absorption spectroscopy (Thermo

241   Fisher 42TL, limit of detection 50 pptv, precision 25 pptv) For each individual experiment, the

242   mixing ratio of NO_2 was kept constant (within the range 34 – 400 ppb) and the aerosol surface

243   area density was varied from zero up to a maximum of 0.04 $m^2\,m^{-3}$. In order to obtain the

244   HONO produced from illuminated aerosol surfaces in the flow tube for a given mixing ratio of

245   NO_2. As well as subtraction of any background HONO, a correction must be made for any loss

246   of HONO owing to its photolysis occurring within the flow tube.

247   In order to determine the rate of photolysis of HONO, the rate of photolysis of NO_2 was first

248   determined using chemical actinometry, and the known spectral output of the lamp and the

249   literature values of the absorption cross-sections and photo-dissociation quantum yields for

250   NO_2 and HONO were used to determine the rate of photolysis of HONO. When just flowing

251   NO_2 in the flow tube, the loss of NO_2 within the illuminated region is determined only by

252   photolysis and is given by:

$$-\frac{d[NO_2]}{dt} = j(NO_2)[NO_2] \tag{3}$$

253   where $j(NO_2)$ is the photolysis frequency of NO_2 for the lamp used in these experiments. From

254   the measured loss of NO_2 in the illuminated region, and with knowledge of the residence time,

255   the photolysis frequency, $j(NO_2)$, was determined to be $(6.43 \pm 0.30) \times 10^{-3}\ s^{-1}$ for the set of

256   experiments using one lamp to illuminate the flow tube. $j(NO_2)$ is given by:

$$j(NO_2) = \int_{\lambda_1}^{\lambda_2} \sigma_\lambda \phi_\lambda F_\lambda\, d\lambda \tag{4}$$

257   where λ_1 and λ_2 represent the range of wavelengths over which the lamp emits, and σ_λ and ϕ_λ

258   are the wavelength-dependent absorption-cross section and photo-dissociation quantum yield

259   of NO_2, respectively, and F_λ is the flux of the lamp at a given wavelength. The flux of the lamp,

260   the spectral intensity of which was measured using a Spectral Radiometer (Ocean Optics QE-

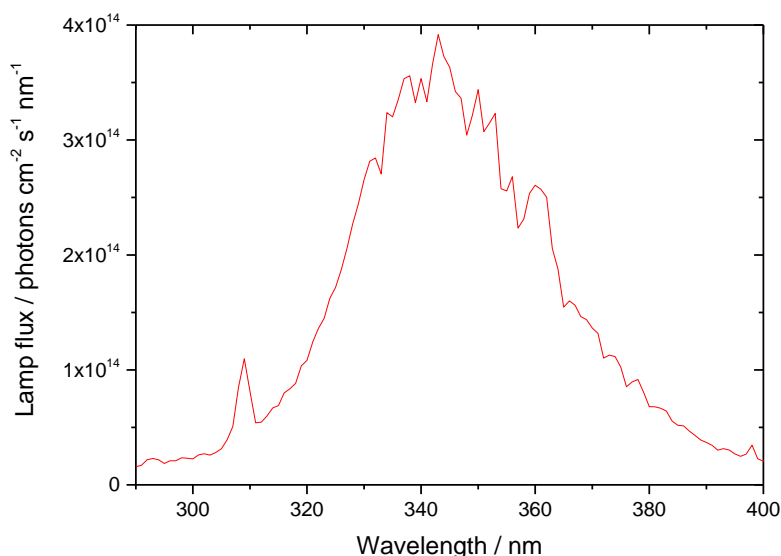261   Pro 500) as a function of wavelength, is shown in Figure 3.

Figure 3. UVA emission spectrum for the 15 W bench lamp used in these experiments between 290-400 nm. The integrated photon flux over this wavelength range is $(1.63 \pm 0.09) \times 10^{16}$ photons cm^{-2} s^{-1} determined from the measured $j(\mathrm{NO_2})$ of $(6.43 \pm 0.30) \times 10^{-3}$ s^{-1}.

262   From the measured $j(\mathrm{NO_2})$, and with knowledge of σ_λ and ϕ_λ for $\mathrm{NO_2}$, the flux of the lamp was

263   determined to be $(1.63 \pm 0.09) \times 10^{16}$ photons cm^{-2} s^{-1} integrated over the 290 – 400 nm

264   wavelength range of the lamp. Using this flux, and the known σ_λ and ϕ_λ for HONO over the

265   same wavelength range, $j(\mathrm{HONO})$ was determined to be $(1.66 \pm 0.10) \times 10^{-3}$ s^{-1}.

266   In the presence of aerosols under illuminated conditions, the rate of heterogeneous removal of

267    $\mathrm{NO_2}$ at the aerosol surface to generate HONO is given by:

$$-\frac{d[\mathrm{NO_2}]}{dt} = k[\mathrm{NO_2}] \tag{5}$$

268   where k is the pseudo-first order rate coefficient for loss of $\mathrm{NO_2}$ at the aerosol surface, and

269   which leads to the generation of HONO. The postulated mechanism for HONO production

270   from $\mathrm{NO_2}$ is discussed in section 3.3.2 below, but for the definition of k it is assumed to be a

271   first order process for $\mathrm{NO_2}$. Integration of equation ((**5**) gives:

$$k = -\frac{\ln\left(\frac{[\mathrm{NO_2}]_0 - [\mathrm{HONO}]_t}{[\mathrm{NO_2}]_0}\right)}{t} \tag{6}$$

11

272   where $[NO_2]_0 - [HONO]_t$ is the concentration of NO_2 at time t, assuming that each NO_2

273   molecule is quantitatively converted to a HONO molecule following surface uptake (see

274   section 3.3.2 for the proposed mechanism), and $[NO_2]_0$ is the initial concentration of NO_2.

275   Hence k can be determined from equation ((**6**) using the measurement of the concentration of

276   HONO, [HONO], that has been generated from TiO_2 aerosol surfaces for an illumination time

277   of t (and after subtraction of any background HONO produced from other sources and after

278   correction for loss via photolysis, see above), and with knowledge of $[NO_2]_0$.

279   The reactive uptake coefficient of NO_2 to generate HONO, $\gamma_{NO_2 \rightarrow HONO}$, defined as the

280   probability that upon collision of NO_2 with the TiO_2 aerosol surface a gas-phase HONO

281   molecule is generated, is given by:

$$\gamma_{NO_2 \rightarrow HONO} = \frac{4 \times k}{v \times SA} \tag{7}$$

282   where v is the mean thermal velocity of NO_2, given by $v = \sqrt{(8RT/(\pi M)}$ with R, T and M as

283   the gas constant, the absolute temperature and the molar mass of NO_2, respectively, SA is the

284   aerosol surface area density ($m^2 m^{-3}$) and k is defined as above. Rearrangement of equation ((**7**)

285   gives:

$$k = \frac{\gamma_{NO_2 \rightarrow HONO} \times SA \times v}{4} \tag{8}$$

286   Figure 4 shows the variation of k, determined from equation ((**6**) above with $t = 52$ s

287   (illumination time in the flow tube), against aerosol surface area density, SA, for $[NO_2]_0 = 200$

288   ppb and RH=15%, from which the gradient using equation (8) yields $\gamma_{NO_2 \rightarrow HONO} = (2.17 \pm$
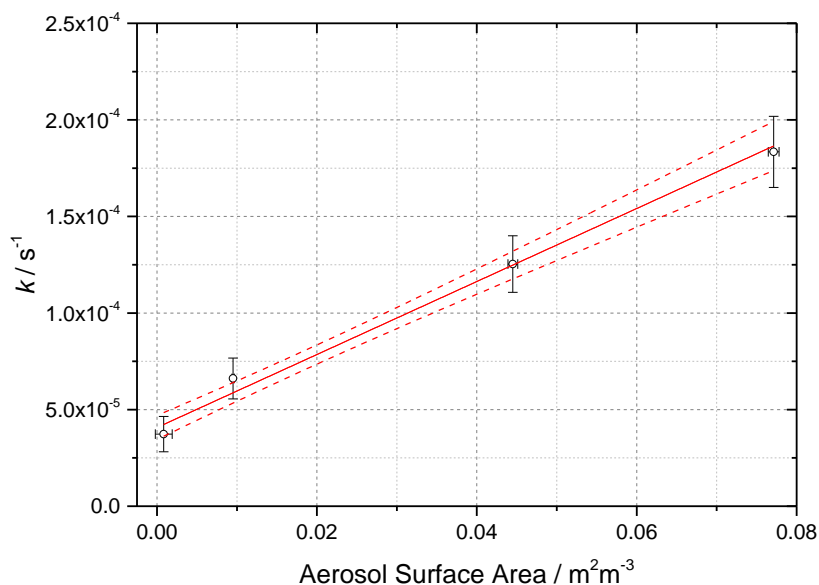
289    $0.09) \times 10^{-5}$.

Figure 4. Pseudo-first-order rate coefficient for HONO production, k (open circles) as a function of aerosol surface area for $[NO_2]=200$ ppb and RH$=15 \pm 1$ %, T $= 293 \pm 3$ K and a photolysis time of 52 ± 2 seconds. The red line is a linear-least squared fit including 1σ confidence bands (dashed lines) weighted to both x and y errors (1σ), the gradient of which yields $\gamma_{NO_2 \rightarrow HONO} = (2.17 \pm 0.09) \times 10^{-5}$, with the uncertainty representing (1σ). The total photon flux of the lamp (see Figure 2 for its spectral output) $= (1.63 \pm 0.09) \times 10^{16}$ photons cm^{-2} s^{-1}.

290 The uncertainty in k (~20 %) shown in Figure 4 and determined by equation ((**6**) is mainly
291 controlled by the uncertainty in the HONO concentration (the HONO signal typically varies
292 between repeated runs for a given SA by ~ 10 % coupled with the 15 % error in calibration
293 factor), the initial NO_2 mixing ratio (10%), and the photolysis time, t (~3 %). The uncertainty
294 in SA is determined by the uncertainty in the SMPS (15%). The error in the value of
295 $\gamma_{NO_2 \rightarrow HONO}$ (typically 20%) is calculated from the 1σ statistical error of the weighted fit shown
296 in Figure 4. An experiment performed using air yielded an uptake coefficient value within 7 %
297 of the equivalent experiment done in N_2, which is well within the experimental error.

298 **2.5 Box model description**

299 A kinetic scheme within the framework of a box model was used together with the differential
300 equation solver Facsimile 4.3.53 (MCPA software Ltd., 2020) to investigate the mechanism of
301 NO_2 adsorption on TiO_2 in the presence of light to produce HONO. The models were only
302 semi-explicit, focusing on determining the stoichiometric amounts of NO_2 needed to produce

303   a single HONO molecule in the gas-phase for comparison with the experimental dependence

304   of HONO production upon NO_2 mixing ratio, and to provide a predictive framework for

305   parameterising the HONO production rate with NO_2 mixing ratio in the atmosphere. Three

306   model scenarios were designed. The simplest model (Model 1) considered only the adsorption

307   of a single molecule of NO_2 to the TiO_2 surface, the surface conversion to HONO in the

308   presence of light and subsequent desorption of HONO, the latter assumed to occur rapidly. The

309   two further model scenarios investigated the effect of a 2:1 stoichiometric relationship between

310   the NO_2 adsorbed to the surface of TiO_2 and the HONO produced, via the formation of an NO_2

311   dimer. Model 2 incorporated an Eley-Rideal mechanism reliant on the adsorption of one NO_2

312   molecule to the surface followed by the subsequent adsorption of a second NO_2 molecule

313   directly onto the first (Figure 5). Model 3, however, features a Langmuir-Hinshelwood

314   mechanism of adsorption in which two NO_2 molecules adsorb to the surface, then diffuse to

315   one another before colliding on the surface and forming the *cis*-ONO-NO_2 dimer (Finlayson-

316   Pitts et al., 2003;de Jesus Madeiros and Pimentel, 2011;Liu and Goddard, 2012;Varner et al.,

317   2014). The formation of the asymmetric *cis*-ONO-NO_2 dimer followed by isomerisation to

318   form the asymmetric *trans*-ONO-NO_2 dimer has been suggested to have an enthalpic barrier

319   that is ~170 kJ mol^{-1} lower than for direct isomerisation to *trans*-ONO-NO_2 from the symmetric

320   N_2O_4 dimer (Liu and Goddard, 2012). The dimerisation of NO_2 and subsequent isomerisation

321   to form *trans*-ONO-NO_2 has been suggested under dark conditions to lead to the formation of

322   both HONO and HNO_3 in the presence of water vapour (Finlayson-Pitts et al., 2003;de Jesus

323   Madeiros and Pimentel, 2011;Liu and Goddard, 2012;Varner et al., 2014). Although the

324   interaction of light with TiO_2 with the concomitant production of electron-hole pairs (R1) is

325   central to HONO formation, we do not specify here the exact mechanism by which the electron-

326   hole pairs interact with surface-bound species to generate HONO. We propose that the

327   interaction with light speeds up the autoionisation of *trans*-ONO-NO_2 to form $(NO^+)(NO_3^-)$,

328   which is represented by reactions R13 and R15 in Models 2 and 3 respectively. $(NO^+)(NO_3^-)$

329   can then react rapidly with surface adsorbed water leading to HONO formation (Varner et al.,

330   2014).

331   A schematic of the proposed mechanism investigated with Models 2 and 3 is shown in Figure

332   5, and consists of (i) the adsorption of NO_2 onto a surface site, (ii) the conversion of NO_2 to

333   form HONO via the formation of an NO_2 dimer intermediate on the surface via either a Eley-

334   Rideal or Langmiur Hinshelwood- type mechanism, (iii) subsequent desorption of HONO from

335   the surface, and finally (iv) competitive removal processes for HONO both on the surface and

336   in the gas-phase that are either dependent or independent on the NO_2 mixing ratio. The model

337   includes the gas-phase photolysis of NO_2 and HONO and the gas phase reactions of both

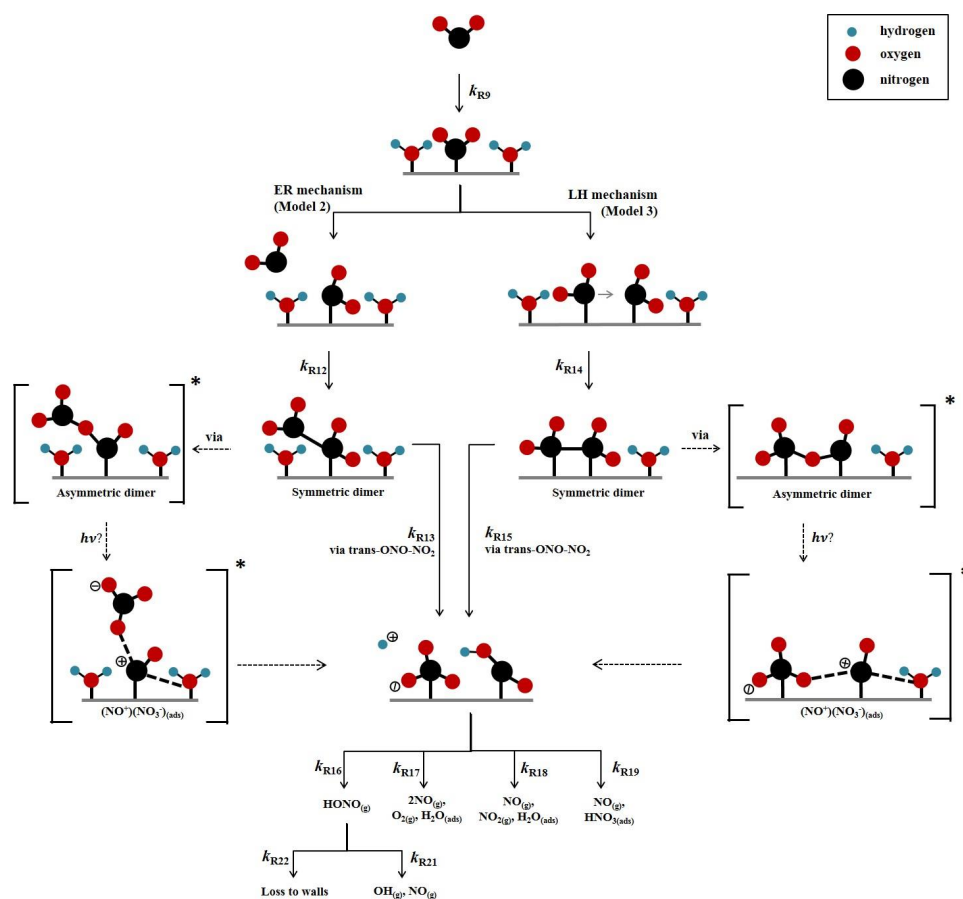338   HONO and NO_2 with OH and $O(^3P)$ atoms.

Figure 5. Schematic diagram of proposed mechanism of uptake of NO_2 on an aerosol surface in the presence
of water to form HONO. Both Eley Rideal, Model 2, and Langmuir Hinshelwood, Model 3, mechanisms are
shown with relevant estimated and calculated rate coefficients used in the models. NO_2 dependent and
independent loss reactions of HONO are also depicted. Nitrogen shown in black, oxygen shown in red and
hydrogen shown in blue. * denotes intermediate steps of the isomerisation of symmetric N_2O_4 to *trans*-ONO-
NO_2 which is then predicted to form HONO.

339   To the best of our knowledge the enthalpy of adsorption of NO_2 onto a TiO_2 surface has not

340   been determined, nor the bimolecular rate coefficients for the chemical steps on the surface

341   shown in Figure 5. Hence, for each of the steps a rate coefficient (s^{-1} or cm^3 molecule^{-1} s^{-1}) was

342   assigned, as given in Table 1, and with the exception of the experimentally determined $j(NO_2)$

343 and the calculated j(HONO), and the gas-phase rate coefficients which are known, the rate
344 coefficients were estimated, with the aim of reproducing the experimental NO_2 dependence of
345 the HONO production and NO_2 reactive uptake coefficient; justification of chosen values is
346 given below.

Reactions	Rate coefficient[d]
Model 1	
R9 $\quad NO_{2(g)} + surface \rightarrow NO_{2(ads)}$	1×10^{-3}
R10 $\quad NO_{2(ads)} \rightarrow HONO_{(ads)}$	1×10^{-3}
R11 $\quad HONO_{(ads)} \rightarrow HONO_{(g)}$	1×10^{-2}
Model 2 and 3	
Model 2 only – Eley-Rideal mechanism	
R12 $\quad NO_{2(g)} + NO_{2(ads)} \rightarrow NO_2 - NO_{2(ads)}$	1×10^{-2}
R13 $\quad NO_2 - NO_{2(ads)} \xrightarrow{via\ trans-ONO-NO_2} HONO_{(ads)} + HNO_{3(ads)}$	5×10^{-3}
Model 3 only – Langmuir-Hinshelwood mechanism	
R14 $\quad NO_{2(ads)} + NO_{2(ads)} \rightarrow NO_{2(ads)} - NO_{2(ads)}$	1×10^{-3}
R15 $\quad NO_{2(ads)} - NO_{2(ads)} \xrightarrow{via\ trans-ONO-NO_2} HONO_{(ads)} + HNO_{3(ads)}$	5×10^{-3}
Common to both Models 2 and 3	
R9 $\quad NO_{2(g)} + surface \rightarrow NO_{2(ads)}$	1×10^{-1}
R16 $\quad HONO_{(ads)} \rightarrow HONO_{(g)}$	5×10^{-2}
R17 $\quad HNO_{3(ads)} + HONO_{(ads)} \rightarrow 2NO_{(g)} + O_{2(g)} + H_2O_{(ads)}$	1×10^{-3}
R18 $\quad HONO_{(ads)} + HONO_{(ads)} \rightarrow NO_{(g)} + NO_{2(g)} + H_2O_{(ads)}$	1×10^{-3}
R19 $\quad NO_{2(g)}(or\ species\ such\ as\ NO_2^+) + HONO_{(ads)} \rightarrow NO_{(g)} + HNO_{3(ads)}$	5×10^{-3}
R20 $\quad NO_{2(g)} + hv \rightarrow NO_{(g)} + O(^3P)_{(g)}$	6×10^{-3a}
R21 $\quad HONO_{(g)} + hv \rightarrow OH_{(g)} + NO_{(g)}$	2×10^{-3b}
R22 $\quad HONO_{(g)} \rightarrow wall\ loss$	1×10^{-4}
R23 $\quad HONO_{(g)} + OH_{(g)} \rightarrow NO_{2(g)} + H_2O_{(g)}$	4.5×10^{-12c}
R24 $\quad NO_{2(g)} + OH_{(g)} \xrightarrow{M} HNO_{3(g)}$	1×10^{-11c}
R25 $\quad O(^3P)_{(g)} + NO_{2(g)} \rightarrow O_{2(g)} + NO_{(g)}$	1×10^{-11c}
R26 $\quad O(^3P)_{(g)} + O_{2(g)} \xrightarrow{M} O_3$	1.5×10^{-14c}
R27 $\quad O(^3P)_{(g)} + NO_{(g)} \xrightarrow{M} NO_{2(g)}$	1.7×10^{-12c}

347 **Table 1.** Reactions included in the chemical mechanism used to model NO_2 uptake onto TiO_2 aerosols. All rate
348 coefficients are estimated, as described in Section 2.5, with the exception of the NO_2 and HONO photolysis rate
349 coefficient and the gas phase rate coefficient which are known. [a]Measured using chemical actinometry with the
350 knowledge of the experimentally determined spectral output of the lamp and the cross-sections and quantum
351 yields of NO_2 and HONO, see section 2.4 for more detail. [b]Calculated using a photon flux of $(1.63 \pm 0.09) \times$

Atmospheric
Chemistry
and Physics
Discussions
Open Access
EGU

352   10^{16} photons cm^{-2} s^{-1}.[c](Sander et al., 2003). [d]Rate coefficients are in the units of s^{-1} for first-order processes or

353   cm^3 molecule^{-1} s^{-1} for second-order processes. T for all k values is 298 K.

354   The modelled Gibbs free energy barrier for the isomerisation of N_2O_4 to form the asymmetric

355   ONO-NO_2 isomer (*cis* or *trans* conformation not specified) was estimated by Pimental et al.,

356   (2007) to be 87 kJ mol^{-1} with a rate coefficient as large as 2×10^{-3} s^{-1} in the aqueous phase at

357   298 K, stated in the study to confirm the Finlayson-Pitts model for the hydrolysis of NO_2 on

358   surfaces via the asymmetric *trans*-ONO-NO_2 dimer (Finlayson-Pitts et al., 2003). Using this

359   study as a guide, we estimated k_{R13} and k_{R15} as 5×10^{-3} s^{-1}, slightly larger than that estimated

360   by Pimental et al., (2007) due to the presence of light. A study into the decomposition of HONO

361   on borosilicate glass surfaces suggested a rate coefficient for the loss HONO on the non-

362   conditioned chamber walls to be $(1.0 \pm 0.2) \times 10^{-4}$ s^{-1} increasing to $(3.9 \pm 1.1) \times 10^{-4}$ s^{-1} when

363   HNO_3 was present on the walls (Syomin and Finlayson-Pitts, 2003). From this we estimated a

364   light-accelerated loss rate coefficient of 1×10^{-3} s^{-1} for the loss of HONO$_{(ads)}$ by reaction with

365   itself, k_{R18}, and through reaction with HNO$_{3(ads)}$, k_{R17}. Both these reactions will occur on the

366   surface of the aerosol. We make the assumption that the rate of loss of HONO to the walls of

367   the chamber for this experiment is less than that of the heterogeneous loss reactions on the

368   photo-catalytic aerosol surface leading to a k_{R22} of 1×10^{-4} s^{-1} as reported by (Syomin and

369   Finlayson-Pitts, 2003). For k_{R12}-k_{R15}, initial values were adopted and were then adjusted to fit

370   the shape of the trend in experimental results of [HONO] and $\gamma_{NO_2 \rightarrow HONO}$ versus [NO_2],

371   discussed fully in Section 3.3.2. For completeness, gas-phase loss reactions of HONO and NO_2

372   with OH and the reactions of O(^{3}P) with NO, NO_2 and O_2 were also included in the model,

373   R23-R27, though their inclusion had no effect on the HONO concentration. The rates of R23-

374   R27 within the model are much smaller than HONO loss reactions on the surface (R17-R19)

375   and the photolysis reactions (R21). For both Models 2 and 3, the adsorption of an NO_2 molecule

376   to the surface, k_{R9}, was assumed to be rapid and not the rate determining step. Likewise, the

377   desorption of HONO was also assumed to be rapid, faster than the loss rates of adsorbed HONO

378   but slower than the adsorption of NO_2; this was necessary for the model to reproduce the trend

379   in the experimental results of [HONO] versus [NO_2], discussed fully in Section 3.3.2.

380   **3   Results and Discussion**

381   **3.1   HONO production from TiO$_2$ aerosol surfaces in the presence of NO$_2$**

382   The production of HONO on TiO$_2$ aerosol surfaces was measured as a function of the initial

383   NO_2 mixing ratio. Figure 6 shows the dependence of the HONO concentration, measured at

384   the end of the flow tube, on the initial NO_2 mixing ratio for an aerosol surface area of $(1.6 \pm$

385    $0.8) \times 10^{-2}$ $m^2\,m^{-3}$. A sharp increase in HONO production at a low mixing ratio of NO_2 was

386   seen followed by a more gradual reduction in HONO production after a peak production at ~
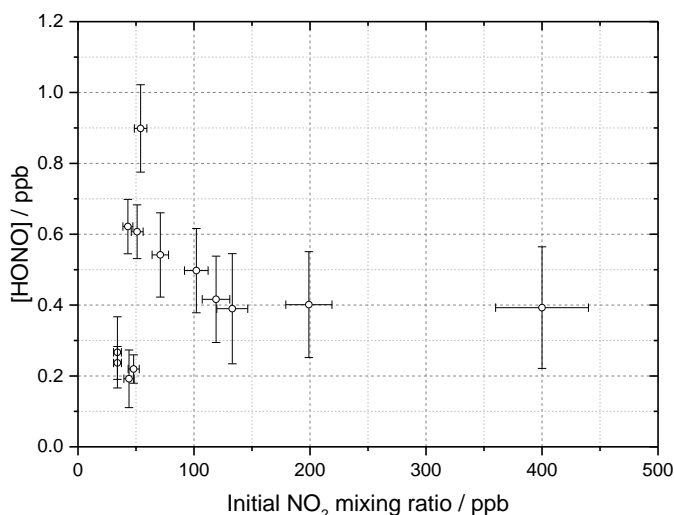
387   54 ± 5 ppb NO_2.

Figure 6. HONO concentration measured at the end of the flow tube as a function of the initial NO_2 mixing ratio, for the aerosol surface area density of $(1.6 \pm 0.8) \times 10^{-2}$ $m^2\,m^{-3}$, relative humidity 15 ± 1 %, photon flux $(1.63 \pm 0.09) \times 10^{16}$ photons $cm^{-2}\,s^{-1}$ (290-400 nm wavelength range), reaction time of 52 seconds and N_2 carrier gas. Each point is an average of up to 20 measurements at the same aerosol surface area and mixing ratio of NO_2. The highest concentration of HONO measured was 0.90 ± 0.12 ppb at $[NO_2] = 54 \pm 5$ ppb. The y error bars represent 1σ while the x error bars represent the sum in quadrature of the errors in the N_2 and NO_2 gas flows and the NO_2 dilution. The SA varied over the experiments at different NO_2 mixing ratios leading to a larger error in the quoted SA.

388   Figure 7 shows the HONO concentration measured at the end of the flow tube over a range of

389   RH values for a fixed aerosol surface area density of $(1.59 \pm 0.16 \times 10^{-2}$ $m^2\,m^{-3})$ and at two

390   NO_2 mixing ratios, displaying a peak in HONO production between 25 – 30 % RH. Above ~

391   37 % RH, for experiments including single-component TiO_2 aerosols, it was found that

392   significant aerosols were lost from the system before entering the flow tube, speculated to be

393   due to loss to the walls of the Teflon lines. As such the RH dependence was only studied up to

394   37 % RH, however a clear drop off in HONO production was seen for both NO_2 mixing ratios
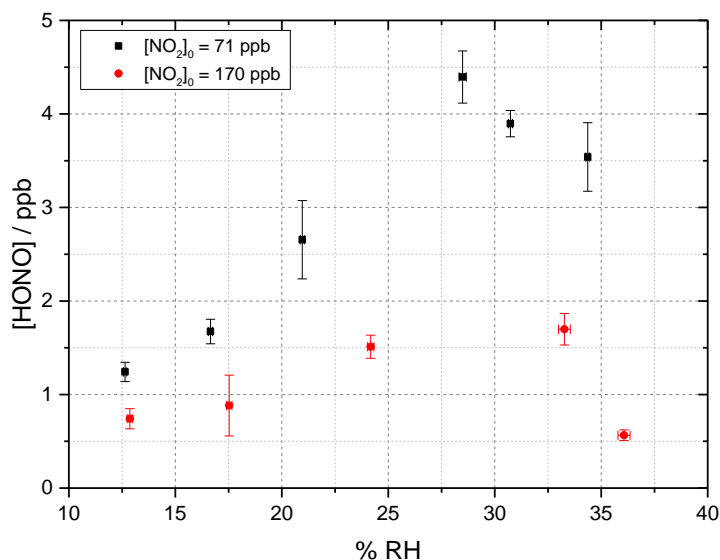
395   studied after ~ 30 % RH.

Figure 7. RH dependence of HONO production from illuminated TiO_2 aerosol surfaces at 295 K in N_2 at 71

(black) and 170 (red) ppb initial NO_2 mixing ratio. The aerosol surface area density was kept constant at (1.59

$\pm$ 0.16) $\times$ 10^{-2} $m^2\,m^{-3}$ with a photon flux of (1.63 $\pm$ 0.09) $\times$ 10^{16} photons $cm^{-2}\,s^{-1}$ and an illumination time of 52

$\pm$ 2 seconds. The error bars represent 1σ.

396   A dependence of HONO production upon RH was expected due to the potential role of water

397   as a proton donor in the production mechanism of HONO on TiO_2 surfaces (R2 and (R5, as

398   shown in Figure 5 (Dupart et al., 2014). The fractional surface coverage of water on the TiO_2

399   aerosol core, V/V_m, at 15 % RH and above was calculated using the parameterisation below,

400   which was determined using transmission IR spectroscopy (Goodman et al., 2001):

$$\frac{V}{V_m} = \left[\frac{c\left(\frac{P}{P_0}\right)}{1 - \left(\frac{P}{P_0}\right)}\right]\left[\frac{1 - (n+1)\left(\frac{P}{P_0}\right)^n + n\left(\frac{P}{P_0}\right)^{n+1}}{1 + (c-1)\left(\frac{P}{P_0}\right) - c\left(\frac{P}{P_0}\right)^{n+1}}\right] \qquad (9)$$

401   where V is the volume of water vapour adsorbed at equilibrium pressure P, V_m is the volume

402   of gas necessary to cover the surface of TiO_2 particles with a complete monolayer, P_0 is the

403   saturation vapour pressure, c is the temperature dependent constant related to the enthalpies of

404   adsorption of the first and higher layers (taken as 74.8 kJ mol^{-1} for TiO$_2$ (Goodman et al., 2001))

405   and n is the asymptotic limit of monolayers (8 for TiO$_2$ (Goodman et al., 2001)) at large values

406   of P/P_0.

407   At 15 % RH, a fractional water coverage of 1.09 was calculated to be present on the surface,

408   increasing to 1.50 at 35 % RH. It has been shown in previous work that HONO can be displaced

409   from a surface by water, leading to an increase in gas-phase HONO with RH (Syomin and

410   Finlayson-Pitts, 2003). The increase in HONO with RH to ~25-30 % RH could therefore be

411   attributed to both an increase in the concentration of the water reactant leading to more HONO

412   formation and the increase in displacement of HONO from the surface due to preferential

413   adsorption of water. A decrease in HONO production seems to occur above ~ 30 % RH, which

414   could be due to the increased water adsorption inhibiting either NO$_2$ adsorption or the

415   electron/hole transfer process (Gustafsson et al., 2006). H$_2$O vapour adsorption is likely

416   enhanced by the superhydrophilic properties of TiO$_2$ surfaces under UV radiation meaning that

417   water monolayers form more quickly on the surface of TiO$_2$ owing to light-induced changes in

418   surface tension (Takeuchi et al., 2005;Gustafsson et al., 2006).

419   At the higher initial concentration of NO$_2$ = 170 ppb, the RH dependence showed a similar

420   peak in HONO production between ~25 - 30 % RH but less HONO was produced overall, as

421   expected from Figure 6 given the higher NO$_2$. Previous work on the production of HONO from

422   suspended TiO$_2$ aerosols reported a strong RH dependence of the uptake coefficient, γ, of NO$_2$

423   to form HONO with a peak at ~ 15 % RH and decreasing at larger RH (Gustafsson et al., 2006).

424   The same trend for the NO$_2$ uptake coefficient was observed by Dupart et al., 2014 on Arizona

425   test dust (ATD) aerosols with a peak in γ at ~ 25 % RH. This increase in the RH at which the

426   uptake coefficient for NO$_2$ in going from TiO$_2$ to ATD aerosols was ascribed to the lower

427   concentration of TiO$_2$ present in ATD aerosols as opposed to single-component TiO$_2$ aerosols

428   used by Gustafsson et al., 2006 as well as by differences in particle size distribution. Gustafsson

429   et al., 2006 reported a larger aerosol size distribution with a bimodal trend with mode diameters

430   of ~ 80 and ~ 350 nm for single-component TiO$_2$ aerosols whereas Dupart et al., 2014 reported

431   a smaller unimodal aerosol size distribution for ATD aerosols with a mode diameter of ~110

432   nm. In this work we also see a larger aerosol size distribution, with a lower mode diameter of

433   ~ 180 nm similar to Dupart et al., 2014 but for pure TiO$_2$ aerosols; aerosol size distribution

434   shown in Figure 2. Similar to the results of Dupart et al., 2014 we observe a trend inversion in

435   [HONO] vs RH at higher RH, between 25-30 %.

436 **3.2 Dependence of reactive uptake coefficient on initial NO₂ mixing ratio**

437 The reactive uptake coefficient, $\gamma_{NO_2 \to HONO}$ for NO₂→HONO on TiO₂ aerosol particles was

438 determined experimentally for 18 different initial NO₂ mixing ratios, and is shown in Figure 8.

439 For each initial NO₂ mixing ratio, the gradient of the first order rate coefficient for HONO

440 production, k, as a function of aerosol surface area density (e.g. Figure 4) and in conjunction

441 with equation ((8), was used to obtain $\gamma_{NO_2 \to HONO}$. The uptake coefficient initially increases

442 with NO₂, reaching a peak at $\gamma_{NO_2 \to HONO} = (1.26 \pm 0.17) \times 10^{-4}$ for an initial NO₂ mixing ratio

443 of 51 ± 5 ppb, before sharply decreasing as the NO₂ mixing ratio continues to increase above
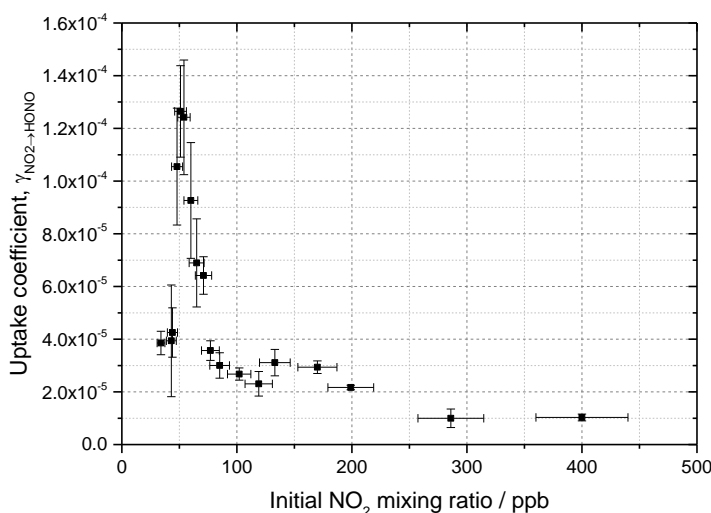
444 this value.

Figure 8 Experimental results showing the reactive uptake coefficients of NO₂ to form HONO, $\gamma_{HONO \to NO_2}$ onto TiO₂ aerosol surfaces as a function of the initial NO₂ mixing ratio. All experiments were conducted in N₂ at 295 K at 15 ± 1 % RH, a photon flux of $(1.63 \pm 0.09) \times 10^{16}$ photons cm⁻² s⁻¹ and an illumination time of 52 ± 2 seconds. $\gamma_{HONO \to NO_2}$ was determined for each NO₂ mixing ratio from the gradient of the pseudo-first-order rate coefficient for HONO production, k, versus aerosol surface area density varied from 0 - 0.04 m² m⁻³ (e.g. as shown in **Figure** 4) and Equation ((8).

445 The increase in uptake coefficient with NO₂ at low NO₂ (< 51 ppb) has not been seen previously

446 in studies of HONO production from TiO₂ containing aerosols with similar [NO₂] ranges

447 (Gustafsson et al., 2006;Ndour et al., 2008;Dupart et al., 2014) or other aerosol surfaces

448 (Bröske et al., 2003;Stemmler et al., 2007). It is worth noting that several of these studies

449   reported the overall uptake of NO_2 onto aerosol surfaces and not specifically the uptake to form

450   HONO, although HONO was indirectly measured in all studies noted here (Gustafsson et al.,

451   2006;Ndour et al., 2008;Dupart et al., 2014). For single-component TiO_2 aerosols, Gustafsson

452   et al., (2006) reported a uptake coefficient, γ_{NO_2}, of 9.6×10^{-4} at 15 % RH and 100 ppb NO_2.

453   Taking into account the HONO yield of 0.75 given by (Gustafsson et al., 2006), an estimated

454    $\gamma_{NO_2 \rightarrow HONO} = 7.2 \times 10^{-4}$ is determined and can be compared to the value observed in this work

455   at 15 % RH and 100 ppb NO_2, ($\gamma_{NO_2 \rightarrow HONO} = (2.68 \pm 0.23) \times 10^{-5}$). The $\gamma_{NO_2 \rightarrow HONO}$ we

456   determine is 27 times smaller than reported by Gustafsson et al., (2006). This difference is

457   mostly due to the lower experimental photon flux in our setup, ~19 times less at $\lambda_{max} = 365$

458   nm owing to the use of one 15 W UV lamp to irradiate the flow tube (Boustead, 2019)

459   compared to Gustafsson et al., 2006 which utilised four 18 W UV lamps.

460   The origins of the increase in $\gamma_{NO_2 \rightarrow HONO}$, together with reaching a maximum and the

461   subsequent decrease at larger NO_2 mixing ratios was investigated using the kinetic box model

462   and postulated mechanism for HONO production described in Section 2.5. The aim was to

463   compare the observed production of HONO and $\gamma_{NO_2 \rightarrow HONO}$ with the modelled values, as a

464   function of NO_2 mixing ratio. The skill of the model to reproduce the observed behaviour

465   enables a validation of the postulated mechanism for HONO production, and variation of the

466   kinetic parameters enables the controlling influence of different steps in the mechanism on

467   HONO production to be evaluated.

468   3.3   Modelling the HONO production mechanism on illuminated TiO_2

### 469   aerosol surfaces

470   The HONO production on illuminated TiO_2 aerosol surfaces was investigated for each of the

471   mechanisms outlined in Table 1.

472   3.3.1   Model 1

473   Model 1 (see Table 1 and Figure 5), which contains the simplest mechanism, was designed to

474   reproduce the decreasing value of the NO_2 uptake coefficient to form HONO, $\gamma_{NO_2 \rightarrow HONO}$, with

475   increasing NO_2 and also the plateauing at higher NO_2 mixing ratios caused by NO_2 reaching a

476   maximum surface coverage, as seen by Stemmler et al., (2007). A decrease in the uptake

477   coefficient of NO_2, γ_{NO_2}, onto dust aerosol surfaces was also seen in studies where the

478   formation of HONO from NO_2 uptake was not directly studied (Ndour et al., 2008;Dupart et

479   al., 2014). The mechanism for Model 1 which is given in Table 1 describes the adsorption of

480   one NO_2 molecule to a surface site which then undergoes the reaction which forms HONO,

481   followed by desorption of HONO to the gas-phase, R9-R11. Any representation of the specific

482   chemical processes which convert NO_2 to HONO on the surface following the initial photo-

483   production of electron-hole pairs in the TiO_2 structure (R2) was not included here as the

484   primary focus was to produce the relationship between $\gamma_{NO_2 \rightarrow HONO}$ and the NO_2 mixing ratio.

485   Gustafsson et al., (2006) reported that the measured rate of photo-induced HONO production

486   is 75% that of the rate of NO_2 removal, whereas the dark disproportionation reaction (**R28**)

487   would predict a 50% yield, and hence that the HONO observed in their studies is not simply a

488   photo-enhancement of:

$$2NO_{2(ads)} + H_2O_{(ads)} \rightarrow HONO_{(g)} + HNO_{3(ads)} \qquad \text{(R28)}$$
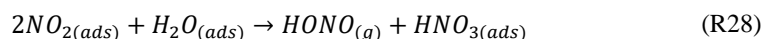
489   Gustafsson et al., (2006) suggests that an oxidant on the surface is produced following the

490   creation of the electron-hole pair (OH is generated in (R2)), and suggests H_2O_2 as a possibility,

491   which is consistent with the observation of OH and HO_2 radicals produced from the surface of

492   illuminated TiO_2 aerosols (Moon et al., 2019). For Model 1, outputs for the predicted

493   concentration of HONO and the reactive uptake coefficient,$\gamma_{NO_2 \rightarrow HONO}$, as a function of initial

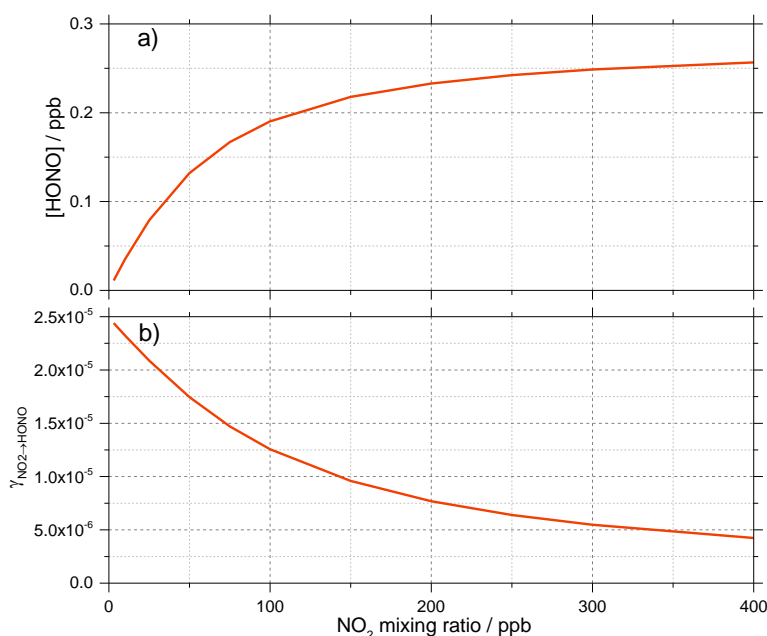494 NO_2 mixing ratio are shown in Figure 9.

Figure 9 Model 1 calculations for (a) the concentration of HONO and (b) the reactive uptake coefficient to form HONO, $\gamma_{NO_2 \rightarrow HONO}$, as a function of NO_2 mixing ratio for a model run time of 52 s. The estimated rate coefficients used in this model are shown in Table 1.

495   For a run time of 52 s, equal to that of the experimental illumination time, Model 1 predicts an

496   increase in HONO production with increasing NO_2 mixing ratio until the HONO concentration

497   begins to plateau, reaching ~0.25 ppb at $[NO_2]$ = 400 ppb, presumably owing to saturation on

498   active aerosol surface sites by NO_2. This leads to the modelled reactive uptake coefficient,

499    $\gamma_{NO_2 \rightarrow HONO}$, monotonically decreasing with increasing NO_2 mixing ratio; a variation in NO_2

500   uptake coefficient similar to that seen in previous photo-enhanced NO_2 aerosol uptake studies

501   (Bröske et al., 2003;Stemmler et al., 2007;Ndour et al., 2008;Dupart et al., 2014). However,

502   the model predictions for Model 1 do not reproduce the experimental variations shown in

503   Figure 6 and Figure 8, in which there is an observed initial rise and then a fall in both the

504   HONO concentration and $\gamma_{NO_2 \rightarrow HONO}$ with increasing NO_2 mixing ratio. Hence, additional

505   processes were considered in the model in order to try to reproduce this behaviour.

506   **3.3.2 Models 2 and 3. Investigating the role of NO_2 dimerisation for the surface**

507   **formation of HONO, and including additional surface losses of HONO**

508   As the experimental $\gamma_{NO_2 \rightarrow HONO}$ increases with NO_2 at low NO_2 (Figure 8), we postulate in

509   Models 2 and 3 that the production of HONO under illuminated conditions is not fully first

510   order in NO_2 and requires more than one NO_2 molecule to form HONO, consistent with the

511   formation of the symmetric NO_2 dimer (N_2O_4) followed by isomerisation on the surface to

512   form the asymmetric *trans*-ONO-NO_2 dimer, which has been suggested to be more reactive

513   with water than the symmetric N_2O_4 dimer (Finlayson-Pitts et al., 2003;Ramazan et al.,

514   2004;Ramazan et al., 2006;Liu and Goddard, 2012) due to the autoionisation to form

515    $(NO^+)(NO_3^-)$ which we propose is accelerated by the presence of light; the full mechanism for

516   which is shown in Figure 5. A recent rotational spectroscopy study found that the *trans*-ONO-

517   NO_2 was better described as the ion pair $(NO^+)(NO_3^-)$ (Seifert et al., 2017). Reaction of the

518    $(NO^+)(NO_3^-)$ ion pair with surface adsorbed water can then lead to the formation of HONO and

519   HNO_3, the feasibility of which is supported by molecular dynamics simulation studies (Varner

520   et al., 2014). While the symmetric N_2O_4 dimer is favoured as it is the most stable conformer,

521   the asymmetric forms have been experimentally observed in several studies (Fateley et al.,

522   1959;Givan and Loewenschuss, 1989b, a, 1991;Pinnick et al., 1992;Forney et al., 1993;Wang

523   and Koel, 1998, 1999;Beckers et al., 2010). A more recent *ab initio* study of NO_2 adsorption

524   at the air-water interface suggested an orientational preference of NO_2 on the surface, with both

525   oxygen atoms facing away from the interface which may imply that the asymmetric dimer

526    $ONO-NO_2$ can form directly, meaning the high barrier between the symmetric and asymmetric

527   forms does not need to be overcome (Murdachaew et al., 2013).

528   The energy barrier to isomerisation of symmetric N_2O_4 in the gas-phase may be reduced due

529   to the interaction with water adsorbed on surfaces. We therefore rule out the dimer in the gas-

530   phase adsorbing onto the surface first, and then reacting to form HONO (Varner et al., 2014).

531   An interesting question is whether the first NO_2 molecule adsorbed to the surface dimerises via

532   the addition of a gaseous NO_2 via an Eley-Rideal (ER) type process, or whether a Langmuir-

533   Hinshelwood (LH) type mechanism is operating in which both NO_2 molecules are first

534   adsorbed and then diffuse together on the surface forming N_2O_4. Both ER and LH mechanisms

535   to form the NO_2 dimer have been included in the model, denoted as Model 2 and Model 3,

536   respectively. The outputs for Models 2 and 3 (see Table 1 for details of the processes included)

537   for the HONO concentration and $\gamma_{NO_2 \rightarrow HONO}$ as a function of NO_2 are shown in Figure 10

538   together with the experimental data. The stoichiometric relationship of the requirement of two

539   NO_2 molecules forming HONO on the surface was key to reproducing the experimental trend

540   of first an increase and then a decrease in both the HONO concentration and the reactive uptake

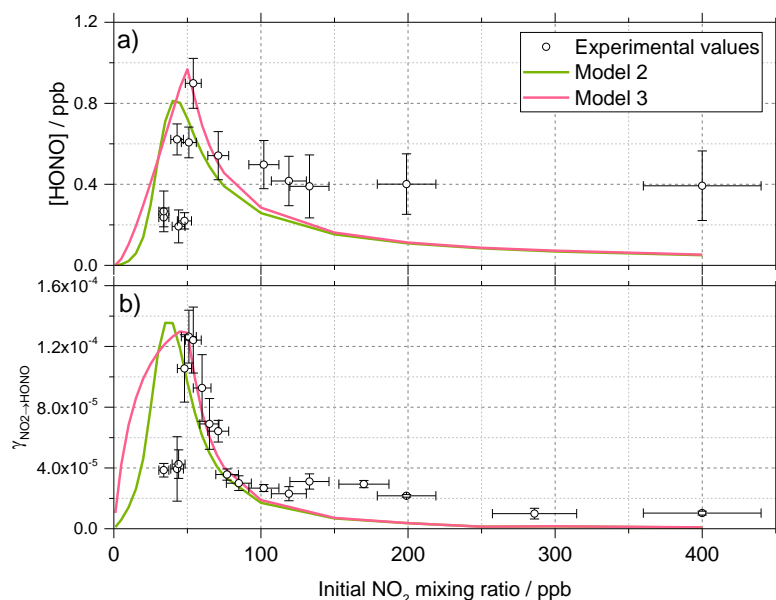541   coefficient with the initial NO_2 mixing ratio.

Figure 10. Experimental values (open circles with 1σ error bars), Model 2 (green line) and Model 3 (pink line) calculations for (a) HONO concentration after 52 s illumination and (b) NO_2 reactive uptake coefficient, $\gamma_{NO_2 \rightarrow HONO}$, as a function of the initial NO_2 mixing ratio. The mechanisms used for these model runs included a 2:1 stoichiometric relationship between the NO_2 adsorbed on the TiO_2 aerosol surface and the HONO produced, as well as additional HONO loss reactions which are dependent on NO_2, see Table 1 for details. Models 2 and use an Eley-Rideal and Langmuir-Hinshelwood mechanisms, respectively, for the formation of the NO_2 dimer on the aerosol surface.

542   In previous work that investigated HONO production from humic acid aerosols, a saturation
543   effect was seen with HONO production plateauing with increasing NO_2 mixing ratio (Stemmler
544   et al., 2007), with the decreasing uptake coefficient, $\gamma_{NO_2 \rightarrow HONO}$, with increasing NO_2 being
545   attributed to NO_2 fully saturating available surface sites. However, the observed decrease of
546   [HONO] at the high NO_2 mixing ratios shown in Figure 8 and Figure 10a suggests that
547   additional reactions on the surface may remove HONO and result in the reduction of [HONO]
548   that is measured. As [HONO] decreases with the increase in the NO_2 mixing ratio, the removal
549   process should either involve NO_2 directly:

$$HONO + NO_2 \rightarrow NO + HNO_3 \qquad (R19)$$
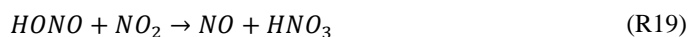
550   or involve species made rapidly from NO_2 on the surface, such as NO_2^+:

$$HONO_{(ads)} + NO_2^+{}_{(ads)} \rightarrow H^+ + 2NO + O_2 \qquad (R19a)$$
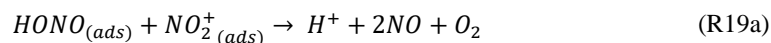
551   which may be present at high enough concentrations of HNO_3 on the surface (Syomin and

552   Finlayson-Pitts, 2003) or following reaction with h_{VB}^+, or a product of the reaction of

553    $O_2^-(or\ e_{CB}^-)$ with NO_2 (R4) i.e. NO_2^-. Transition state theory (TST) studies of the gas-phase

554   reaction of HONO with NO_2 to form HNO_3 calculated a large activation energy which varied

555   depending on whether the reaction occurs via O abstraction by HONO (159 kJ mol^{-1}) or via

556   OH abstraction via NO_2 (~133-246 kJ mol^{-1})(Lu et al., 2000). In the gas-phase these reactions

557   are too slow to be important but they could be enhanced on the surface, potentially more so on

558   a photoactive surface such as TiO_2. The NO_2 dependent loss reaction, k_{R19} in Table 1, was

559   necessary in the model to reproduce the sharp decrease in [HONO] versus NO_2 seen

560   experimentally after ~54 ppb NO_2. Without k_{R19} the modelled [HONO] continued to increase

561   to a plateau, as seen in Model 1 (see Figure 9). In order to observe the model output seen in

562   Figure 10 for model 2 and 3, k_{R19} also had to be slower than the desorption of HONO from the

563   surface, k_{R16}.

564   The addition of an NO_2 dependent loss reaction to both Model 2 and 3 had the most significant

565   effect on the trend in modelled HONO concentration. Though it is also possible that a

566   secondary product could remain adsorbed and therefore block active sites on the TiO_2 surface,

567   effectively poisoning the photo-catalyst, NO_2 independent loss reactions in the model, k_{R17} and

568   k_{R18} had little effect on the trend in [HONO] vs NO_2, only having an effect on the overall

569   [HONO]. HNO_3 has however been shown to remain adsorbed to surfaces once formed

570   (Sakamaki et al., 1983;Pitts et al., 1984;Finlayson-Pitts et al., 2003;Ramazan et al., 2004) and

571   may also react with adsorbed HONO, further reducing the product yield (Finlayson-Pitts et al.,

572   2003): these NO_2 independent loss reactions may therefore become more important at higher

573   NO_2 concentrations and hence surface concentrations of HONO and HNO_3:

$$HONO_{(ads)} + HNO_{3(ads)} \rightarrow 2NO_{(g)} + H_2O_{(ads)} + O_{2(g)} \qquad (R17)$$
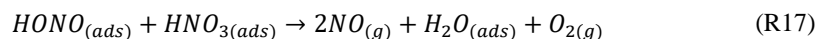
574   The photolysis of particulate nitrate was not considered in Models 2 or 3, due to the lack of

575   particulate nitrate in the system at t=0. The gas-to-particle conversion of any HNO_3 formed

576   was not considered to be important due to the assumption that most HNO_3 formed would

577   remain adsorbed to the aerosol surface (Sakamaki et al., 1983;Pitts et al., 1984;Finlayson-Pitts

578   et al., 2003;Ramazan et al., 2004).

579   For Model 2, which includes the production of HONO via the Eley-Rideal mechanism, in order

580   to reproduce the experimentally observed sharp increase followed by a decrease in both

581   [HONO] and $\gamma_{NO_2 \rightarrow HONO}$ as a function of increasing NO_2 mixing ratio, the modelled rate

582   coefficient for the adsorption of a gas-phase NO_2 molecule to another the surface adsorbed

583   NO_2 to initially form the symmetric N_2O_4 dimer, k_{R12}, had to be larger than for the isomerisation

584   step to form HONO and HNO_3 via *trans*-ONO-NO_2, k_{R13}. Interestingly, for HONO production

585   via the Langmuir-Hinshelwood mechanism, Model 3, the modelled rate coefficient for the

586   diffusion of one NO_2 molecule across the surface to form the dimer with another NO_2 molecule,

587   k_{R14}, had to be smaller than for the isomerisation step, k_{R15}, to more closely represent the

588   experimental results for the uptake coefficient. Additionally, in order to reproduce the

589   experimental trend in HONO formation as a function of NO_2 mixing ratio, the rate coefficient

590   for the NO_2 dependent loss reaction, k_{R19}, had to be larger than the NO_2 independent reactions,

591   k_{R17} and k_{R18}, leading to $k_{R19} = 5 \times 10^{-3}$ s^{-1}. The modelled HONO concentration also sensitive

592   to the active site surface concentration: Model 3 required an active site surface concentration

593   2.5 times that of Model 2 to reproduce the peak in [HONO] at ~ 51 ppb NO_2 observed in the

594   experimental results. The reason for this is due to the difference in active site occupation in the

595   2 models: one active site is being occupied by two NO_2 molecules per HONO formed in Model

596   2 as opposed to Model 3 where two active sites are occupied per HONO formed. Regardless

597   of the choice of an Eley Rideal or Langmuir Hinshelwood mechanism, both models reproduce

598   the general shape of [HONO] and $\gamma_{NO_2 \rightarrow HONO}$ with NO_2, providing evidence that two NO_2

599   molecules are required to form HONO.

600   ## 3.4   HONO production from illumination of a mixed NH$_4$NO$_3$/TiO$_2$ aerosol

601   ##   in the absence of NO$_2$

602   The photolysis of particulate nitrate has been postulated as a source of HONO under ambient

603   sunlit conditions during several field campaigns, from both aircraft and ground based

604   measurements (Reed et al., 2017;Ye et al., 2017a;Ye et al., 2017b). Here, experiments were

605   carried out to investigate the formation of HONO from particulate nitrate photolysis, with and

606   without the addition of a photo-catalyst. This is of significant interest for marine environments

607   downwind of arid desert regions due to the availability of TiO_2 or other photocatalytic materials

608   within aerosols in dust plumes that are transported from these regions (Hanisch and Crowley,

609   2003).

610   Using the aerosol flow tube setup described in Sections 2.1-2.4, an aqueous solution of

611   ammonium nitrate (5 g NH_4NO_3 in 500 ml milli-Q water) was used to generate nitrate aerosols.

612   At the RH used in this experiment, ~ 50 %, the aerosols were still deliquesced. For these

613   experiments the residence time of the aerosols in the illuminated region of the flow tube was

614   30 seconds (flow rate ~ 6 lpm), with the production of HONO following illumination measured

615   as a function of aerosol surface area density. The number of lamps was increased from 1 to 4,

616   increasing the photon flux from $(1.63 \pm 0.09) \times 10^{16}$ to $(8.21 \pm 2.39) \times 10^{16}$ photons cm^{-2} s^{-1}

617   and $j(NO_2)$ from $(6.43 \pm 0.30) \times 10^{-3}$ to $(3.23 \pm 0.92) \times 10^{-2}$ s^{-1}. The $j(NO_2)$, $j(HONO)$ and flux

618   values for 4 lamps were more than 4 times that of 1 lamp only due to the lamp casings being

619   mirrored, and so with 4 lamps, with 2 lamps on either side of the flow tube, the casings reflected

620   the light back into the flow tube, increasing the effective light intensity. For these experiments,

621   no gaseous NO_2 was added to the gas entering the flow tube. As shown in Figure 11, for the

622   illumination of pure nitrate aerosols, although a small amount of HONO was observed at higher

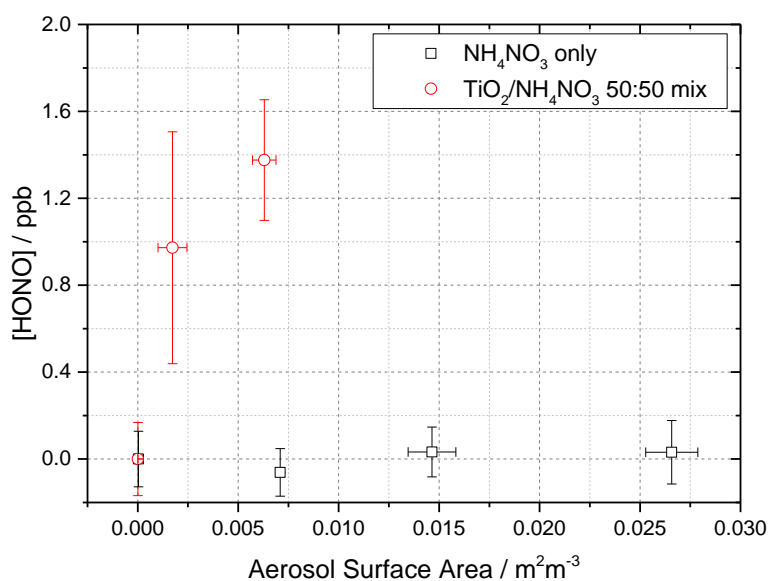623   aerosol loadings, no statistically significant production of HONO was seen.

Figure 11. Dependence of the HONO concentration generated as a function of aerosol surface area density for pure NH_4NO_3 aerosol (black open squares, error bars represent 1σ) and 1:1 TiO_2/NH_4NO_3 mixed aerosol (red open circles, error bars represent 1σ). Both experiments were performed in N_2 at 295 K, an illuminated residence time of 30 s, and a lamp photon flux of $(8.29 \pm 2.39) \times 10^{16}$ photons cm^{-2} s^{-1}. The NH_4NO_3 only experiment was performed at ~50 ± 5 % RH while the TiO_2/NH_4NO_3 mix experiment was performed at 20 ± 2

% RH. For all points, the background HONO seen observed without illumination has been subtracted. At zero aerosol surface area density there is no HONO generated from the walls of the flow tube.

624   A second set of experiments were performed with an aqueous solution of titanium dioxide and

625   ammonium nitrate combined in a 1:1 mass ratio to give a TiO_2/NH_4NO_3 aerosol mixture (5 g

626   NH_4NO_3 and 5 g TiO_2 in 500 ml milli-Q water) to investigate if the photo-catalytic properties

627   of TiO_2 facilitate the production of HONO in the presence of nitrate. The RH was decreased to

628   ensure the maximum TiO_2 photocatalytic activity (Jeong et al., 2013). A recent study using

629   Raman micro spectroscopy to observe phase changes in salt particles reported an efflorescence

630   point of pure ammonium nitrate to be between 13.7-23.9 % RH (Wu et al., 2019). It is possible

631   therefore that at the RH used in this experiment, ~ 20 %, the aerosols were still deliquesced.

632   As shown in Figure 11, the presence of TiO_2 in the aerosol mixture showed a significant

633   production of HONO without the presence of NO_2, a potentially significant result for the

634   production of HONO in low NO_x environments in the presence of mixed dust/nitrate aerosols,

635   for example in oceanic regions off the coast of West Africa, or in continental regions impacted

636   by outflow from the Gobi desert. Using the Aerosol Inorganic Model (AIM) (Clegg et al.,

637   1998;Wexler and Clegg, 2002), the nitrate content of the aerosol at 50 % RH was calculated.

638   From this and the aerosol volume distribution given by the SMPS, the $[NO_3^-]$ within the

639   aerosols could be calculated. The formation of HONO by photolysis of particulate nitrate is

640   given by:

$$\frac{d[\text{HONO}]}{dt} = j(\text{pNO}_3)[\text{NO}_3^-] \tag{10}$$

641   and hence:

$$[\text{HONO}] = j(\text{pNO}_3)[\text{NO}_3^-]t \tag{11}$$

642   where $j(\text{pNO}_3)$ is the photolysis frequency of nitrate for the lamps used in these experiments

643   and t is the illumination time of the experiment. With knowledge of [HONO], $[NO_3^-]$ and $t =$

644   30 s, $j(\text{pNO}_3)$ can be calculated from a measurement of [HONO] as a function of $[NO_3^-]$, as

645   shown in Figure 12, for the mixed nitrate/ TiO_2 experiment.
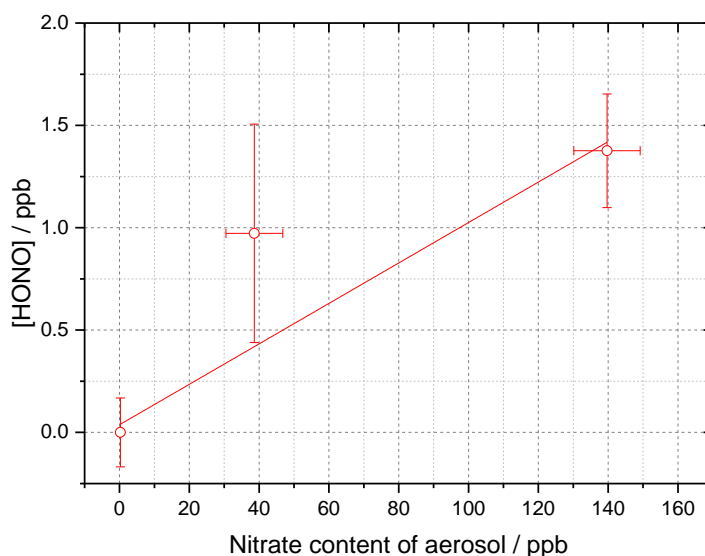
Figure 12. Dependence of [HONO] on the calculated nitrate concentration in the aerosol (using the AIM model) for the mixed TiO_2/ammonium nitrate aerosol experiment. Using Equation (**10**and for $t = 30$ s, the gradient gives $j(pNO_3) = (3.29 \pm 0.89) \times 10^{-4}$ s^{-1}. Experiment performed at 15 ± 1 % RH, in N_2 at 295 K with a lamp photon flux of $(8.29 \pm 2.39) \times 10^{16}$ photons cm^{-2} s^{-1}. For all points, the background HONO seen observed without illumination has been subtracted.

646   When using the 4 lamps together, the experimental particulate nitrate photolysis rate, $j(pNO_3)$,

647   was determined to be $(3.29 \pm 0.89) \times 10^{-4}$ s^{-1} for the mixed nitrate/TiO_2 aerosol. From this, it

648   is possible to estimate $j(pNO_3)$ for ambient conditions typical of the tropical marine boundary

649   layer. Taking the ratio of the experimental $j(HONO)$ for 4 lamps $((8.35 \pm 0.18) \times 10^{-3}$ s$^{-1})$ and

650   the measured $j(HONO)$ from the RHaMBLe campaign held at the Cape Verde Atmospheric

651   Observatory [May-June,2007] $(1.2 \times 10^{-3}$ s$^{-1})$ (Carpenter et al., 2010;Whalley et al., 2010;Reed

652   et al., 2017) and assuming that $j(pNO_3)$ and $j(HONO)$ scale in the same way, ambient $j(pNO_3)$

653   can be determined from:

$$j(pNO_3)_N = j(pNO_3) \times \frac{1.2 \times 10^{-3}}{j(HONO)} \tag{12}$$

654   where $j(pNO_3)_N$ is the photolysis rate coefficient of particulate nitrate at Cape Verde, $j(pNO_3)$

655   is the experimentally determined photolysis rate coefficient of particulate nitrate to form

656   HONO and j(HONO) is the HONO photolysis rate coefficient calculated from the

657   experimentally determined j(NO$_2$).

658   Using j(pNO$_3$) = $(3.29 \pm 0.89) \times 10^{-4}$ s^{-1}, the rate of HONO production from nitrate photolysis

659   at Cape Verde was calculated to be j(pNO$_3$)$_N$ = $(4.73 \pm 1.01) \times 10^{-5}$ s^{-1} from the mixed

660   nitrate/TiO$_2$ aerosol experiment. Although for pure nitrate aerosol in the absence of TiO$_2$ the

661   data were scattered and the HONO production small (Figure 11), an upper limit estimate of

662   j(pNO$_3$)$_N$ = $(1.06 \pm 1.15) \times 10^{-6}$ s^{-1} under conditions at Cape Verde could be made using

663   equation (11), as done for rate of HONO production from mixed nitrate/TiO$_2$ aerosols. The

664   atmospheric implications of this will be considered below.

665   ## 4   Implications of HONO production from TiO$_2$ for tropospheric chemistry

666   ### 4.1   Production of HONO from sunlight aerosols containing TiO$_2$ in the

667   presence of NO$_2$

668   For the reactive uptake of NO$_2$ onto illuminated TiO$_2$ particles as a function of the initial NO$_2$

669   mixing ratio, as shown in Figure 8, a maximum value of $\gamma_{NO_2 \rightarrow HONO} = (1.26 \pm 0.17) \times 10^{-4}$

670   was determined at 51 ± 5 ppb NO$_2$ for a photon flux from the lamp of $(1.63 \pm 0.09) \times 10^{16}$

671   photons cm^{-2} s^{-1}. These experiments were for single-component TiO$_2$ particles, and so for dust

672   aerosols a value of $\gamma_{NO_2 \rightarrow HONO} = (1.26 \pm 0.17) \times 10^{-5}$ is appropriate assuming a 10 % fraction

673   of TiO$_2$ and/or other photoactive materials (which behave similarly for HONO production) in

674   mineral dust (Hanisch and Crowley, 2003). Dust aerosols are transported from the Gobi desert

675   to urban areas of China where high NO$_x$ and nitrate aerosol concentrations have been observed

676   and in these areas HONO production facilitated by photo-catalysts may be important (Saliba

677   et al., 2014).

678   Using an average daytime maximum for [NO$_2$], j(NO$_2$) and aerosol surface area measurements

679   for a non-haze period in May-June in 2018 in Beijing, of 50 ppb, 1×10^{-2} s^{-1} and 2.5×10^{-3} m^2

680   m^{-3} (of which a maximum of 0.3 % was assumed to be TiO$_2$, though this could be higher in

681   dust impacted events (Schleicher et al., 2010)) respectively, a production rate of HONO of 1.70

682    $\times 10^5$ molecules cm^{-3} s^{-1} (~24.8 ppt h^{-1}) has been estimated using the maximum reactive uptake

683   coefficient measured in this work, $\gamma_{NO_2 \rightarrow HONO} = (1.26 \pm 0.17) \times 10^{-4}$. The lamp used to

684   illuminate the TiO$_2$ aerosols in these experiments gives rise to j(NO$_2$) = $(6.43 \pm 0.3) \times 10^{-3}$ s^{-1},

685   and so $\gamma_{NO_2 \rightarrow HONO}$ has been scaled by a factor of 1.55 to match the noon j(NO$_2$) measured in

686   May-June 2018 in Beijing (10^{-2} s^{-1}), to take into account the relatively small difference in

Atmospheric
Chemistry
and Physics
Discussions

Open Access

EGU

687 experimental and atmospheric photon flux for Beijing. The HONO production rate estimated

688 here for noontime summer [May-June 2018] in Beijing (~25 ppt hr^{-1}) is similar to the value for

689 the maximum production of HONO from urban humic acid aerosol surfaces in Europe, 17 ppt

690 h^{-1} at 20 ppb NO_2 reported by Stemmler et al., 2007. For comparison, the net gaseous

691 production rate of HONO at noon in May-June 2018 Beijing was determined from the

692 measured rate of gas-phase production and losses:

$$P_{HONO} = k_{OH+NO}[OH][NO] - (j(HONO) \times [HONO] + k_{OH+HONO}[OH][HONO]) \quad (13)$$

693 where $k_{OH+NO} = 3.3 \times 10^{-11}$ cm^3 molecule^{-1} s^{-1} (Atkinson et al., 2004), $k_{OH+HONO} = 6 \times 10^{-12}$

694 cm^3 molecule^{-1} s^{-1} (Atkinson et al., 2004) and j(HONO)=1×10^{-2} s^{-1} for an average maximum

695 noontime OH concentration of 8×10^6 molecules cm^{-3} (Whalley et al., 2020), NO

696 concentration of 1.45 ppb (Whalley et al., 2020) and HONO concentration of 0.8 ppb (Whalley

697 et al., 2020).

698 The net gas-phase production of HONO from Equation (13 was calculated to be -3.8 ppb hr^{-1}

699 (a net loss) as expected due to HONO loss by photolysis peaking at solar noon, suggesting the

700 production of HONO heterogeneously from TiO_2 and NO_2 (~25 ppt hr^{-1}) would have little

701 effect on the overall HONO budget for Beijing summertime at noon.

702 4.2 Production of HONO from photolysis of mixed dust/nitrate aerosols

703 Oceanic environments, for example the Atlantic Ocean which is impacted by both dust aerosols

704 from the Sahara and high concentrations of mixed nitrate aerosols from sea spray, and despite

705 low NO_2 concentrations could be important for particulate nitrate photolysis as a source of

706 HONO (Hanisch and Crowley, 2003;Ye et al., 2017b). From the particulate nitrate photolysis

707 experiments in the absence of NO_2 conducted here, a $j(pNO_3)_N = (4.73 \pm 1.01) \times 10^{-5}$ s^{-1} was

708 determined in the presence of the TiO_2 photo-catalysts (Section 3.4). Using the experimental

709 j(pNO$_3$), scaled to typical ambient light levels, and a mean noon concentration of nitrate

710 aerosols of 400 ppt measured at Cape Verde (Reed et al., 2017), taken as an example marine

711 boundary layer environment with a high concentration of mineral dust aerosols, a rate of

712 HONO production from particulate nitrate at Cape Verde was calculated as 4.65×10^5

713 molecule cm^{-3} s^{-1} (68 ppt hr^{-1}). We note that this value would be ~ 50 times smaller for pure

714 nitrate aerosols. The missing rate of HONO production i.e. not taken into account by the gas

715 phase production and loss, P_{other}, from the Cape Verde RHaMBLe campaign, can be calculated

716 using the observed HONO concentration, [HONO] and the known gas-phase routes for HONO

717 production and loss:

$$P_{other} = ([HONO](j(HONO) + k_{OH+HONO}[OH])) - (k_{OH+NO}[OH][NO])) \qquad (14)$$

718 where $k_{OH+NO} = 3.3 \times 10^{-11}$ cm^3 molecule^{-1} s^{-1} (Atkinson et al., 2004), $k_{OH+HONO} = 6 \times 10^{-12}$

719 cm^3 molecule^{-1} s^{-1} (Atkinson et al., 2004) and $j(HONO)=2 \times 10^{-3}$ s^{-1} for average maximum

720 measured concentrations of 1×10^7 molecules cm^{-3} for OH (Whalley et al., 2010), 5.41×10^7

721 molecule cm^{-3} for NO (Whalley et al., 2010) and 1.23×10^8 molecule cm^{-3} for HONO (Whalley

722 et al., 2010).

723 Using Equation (14) this missing HONO production rate for Cape Verde was 34.6 ppt hr^{-1},

724 which is within a factor of two of the rate of HONO production (68 ppt hr-1) calculated from

725 nitrate photolysis using our experimental HONO production data for mixed nitrate/TiO$_2$

726 aerosols. These results provide further evidence that particulate nitrate photolysis in the

727 presence of photocatalytic compounds such as TiO$_2$ found in dust could be significant in

728 closing the HONO budget for this environment (Whalley et al., 2010;Reed et al., 2017;Ye et

729 al., 2017a).

730 **5   Conclusions.**

731 The experimental production of HONO from both illuminated TiO$_2$ aerosols in the presence of

732 NO$_2$ and from mixed nitrate/TiO$_2$ aerosols in the absence of NO$_2$ was observed, with the

733 HONO concentrations measured using photo-fragmentation laser-induced fluorescence

734 spectroscopy. Using experimental data, the reactive uptake of NO$_2$ onto the TiO$_2$ aerosol

735 surface to produce HONO, $\gamma_{NO_2 \rightarrow HONO}$, was determined for NO$_2$ mixing ratios ranging from

736 34 to 400 ppb, with a maximum $\gamma_{NO_2 \rightarrow HONO}$ value of $(1.26 \pm 0.17) \times 10^{-4}$ for single-component

737 TiO$_2$ aerosols observed at 51 ppb NO$_2$, and for a lamp photon flux of $(1.65 \pm 0.02) \times 10^{16}$

738 photons cm^{-2} s^{-1} (integrated between 290 and 400 nm). The measured reactive uptake

739 coefficient, $\gamma_{NO_2 \rightarrow HONO}$, showed an increase then subsequent decrease as a function of NO$_2$

740 mixing ratio, peaking at 51 ± 5 ppb. Box modelling studies supported a mechanism involving

741 two NO$_2$ molecules on the aerosol surface per HONO molecule generated, providing evidence

742 for the formation of a surface-bound NO$_2$ dimer intermediate. The exact mechanism for HONO

743 formation, for examples the step(s) which are accelerated in the presence of light, remains

744 unclear, although previous studies would suggest the process occurs via the isomerisation of

745 the symmetric N$_2$O$_4$ dimer to give *trans*-ONO-NO$_2$, either via *cis*-ONO-NO$_2$ or directly,

746 suggested to be more reactive with water than the symmetric dimer (Finlayson-Pitts et al.,

747 2003;Ramazan et al., 2004;Ramazan et al., 2006;de Jesus Madeiros and Pimentel, 2011;Liu

748 and Goddard, 2012;Murdachaew et al., 2013;Varner et al., 2014). Investigations into the RH

749   dependence of the HONO production mechanism on TiO_2 aerosols showed a peak in

750   production between ~25-30 % RH, with lower HONO production at higher NO_2 mixing ratios

751   observed for all RHs tested. The increase in HONO production with increasing RH can be

752   attributed to a higher concentration of H_2O on the surface increasing its availability for the

753   hydrolysis reaction to give HONO, whereas a decrease in HONO production after RH ~ 30 %

754   could be due to the increased water surface concentration inhibiting the adsorption of NO_2.

755   Using the laboratory reactive uptake coefficient for HONO production, $\gamma_{NO_2 \rightarrow HONO}$, the rate of

756   production of HONO from illuminated aerosols in Beijing in summer for typical NO_2 mixing

757   ratios and aerosol surface areas was found to be similar to that estimated previously for the

758   production of HONO from urban humic acid aerosol surfaces in Europe.

759   In the absence of NO_2, significant HONO production from 50:50 mixed nitrate/TiO_2 aerosols

760   was measured. Using the experimental HONO concentrations observed, a rate of HONO

761   production from nitrate photolysis was calculated, which was then scaled to the ambient

762   conditions encountered at the Cape Verde Atmospheric Observatory in the tropical marine

763   boundary layer. A HONO production rate of 68 ppt hr^{-1} for the mixed nitrate/TiO_2 aerosol was

764   found for CVAO conditions, similar in magnitude to the missing HONO production rate that

765   had been calculated previously in order to bring modelled HONO concentrations into line with

766   field-measured values at CVAO. These results provide further evidence that aerosol particulate

767   nitrate photolysis may be significant as a source of HONO, and hence NO_x, in the remote

768   marine boundary layer, where mixed aerosols containing nitrate and a photo-catalytic species

769   such as TiO_2, as found in dust, are present.

770   However, the production of HONO from pure, deliquesced ammonium nitrate aerosols alone

771   could not be definitively confirmed over the range of conditions used in our experiments,

772   suggesting that another component within the aerosol is necessary for HONO production.

773   Future work should be directed towards studying pure nitrate aerosols over a wider range of

774   conditions, for example varying the aerosol pH, and also adding other chemical species into

775   the aerosol which may promote HONO production.

776   *Data availability.* Data presented in this study can be obtained from authors upon request

777   (d.e.heard@leeds.ac.uk)

778   *Competing interests.* The authors declare that they have no conflict of interest.

References

783 Alicke, B., Platt, U., and Stutz, J.: Impact of nitrous acid photolysis on the total hydroxyl radical
784 budget during the Limitation of Oxidant Production/Pianura Padana Produzione di Ozono
785 study in Milan, J. Geophys. Res. Atmos., 107, https://doi.org/10.1029/2000JD000075, 2002.

786 Atkinson, R., Baulch, D. L., Cox, R. A., Crowley, J. N., Hampson, R. F., Hynes, R. G., Jenkin,
787 M. E., Rossi, M. J., and Troe, J.: Evaluated kinetic and photochemical data for atmospheric
788 chemistry: Volume I - gas phase reactions of O_x, HO_x, NO_x and SO_x species, Atmos. Chem.
789 Phys., 4, 1461-1738, https://doi.org/10.5194/acp-4-1461-2004, 2004.

790 Beckers, H., Zeng, X., and Willner, H.: Intermediates involved in the oxidation of nitrogen
791 monoxide: Photochemistry of the cis-$N_2O_2 \cdot O_2$ complex and of sym-N_2O_4 in Solid Ne Matrices,
792 Chemistry–A European Journal, 16, 1506-1520, https://doi.org/10.1002/chem.200902406,
793 2010.

794 Boustead, G. A.: Measurement of nitrous acid production from aerosol surfaces using Photo-
795 Fragmentation Laser-Induced Fluorescence, School of Chemistry, University of Leeds, 2019.

796 Bröske, R., Kleffmann, J., and Wiesen, P.: Heterogeneous conversion of NO_2 on secondary
797 organic aerosol surfaces: A possible source of nitrous acid (HONO) in the atmosphere?, Atmos.
798 Chem. Phys., 3, 469-474, https://doi.org/10.5194/acp-3-469-2003, 2003.

799 Cantrell, C., Zimmer, A., and Tyndall, G. S.: Adsorption cross sections for water vapor from
800 183 to 193 nm, Geophys. Res. Lett., 24, 2195-2198, https://doi.org/10.1029/97GL02100, 1997.

801 Carpenter, L. J., Fleming, Z. L., Read, K. A., Lee, J. D., Moller, S. J., Hopkins, J. R., Purvis,
802 R. M., Lewis, A. C., Müller, K., Heinold, B., Herrmann, H., Fomba, K. W., van Pinxteren, D.,
803 Müller, C., Tegen, I., Wiedensohler, A., Müller, T., Niedermeier, N., Achterberg, E. P., Patey,
804 M. D., Kozlova, E. A., Heimann, M., Heard, D. E., Plane, J. M. C., Mahajan, A., Oetjen, H.,
805 Ingham, T., Stone, D., Whalley, L. K., Evans, M. J., Pilling, M. J., Leigh, R. J., Monks, P. S.,
806 Karunaharan, A., Vaughan, S., Arnold, S. R., Tschritter, J., Pöhler, D., Frieß, U., Holla, R.,
807 Mendes, L. M., Lopez, H., Faria, B., Manning, A. J., and Wallace, D. W. R.: Seasonal
808 characteristics of tropical marine boundary layer air measured at the Cape Verde Atmospheric
809 Observatory, Journal of Atmospheric Chemistry, 67, 87-140, https://doi.org/10.1007/s10874-
810 011-9206-1, 2010.

811 Chen, H., Nanayakkara, C. E., and Grassian, V. H.: Titanium dioxide photocatalysis in
812 atmospheric chemistry, Chem. Rev., 112, 5919-5948, https://doi.org/10.1021/cr3002092,
813 2012.

814 Clegg, S. L., Brimblecombe, P., and Wexler, A. S.: Thermodynamic model of the system H^+-
815 $NH_4^+- Na^+- SO_4^{2-}- NO_3^-- Cl^-- H_2O$ at 298.15 K, J. Phys. Chem. A, 102, 2155-2171,
816 https://doi.org/10.1021/jp973043j, 1998.

817 Crilley, L. R., Kramer, L. J., Ouyang, B., Duan, J., Zhang, W., Tong, S., Ge, M., Tang, K., Qin,
818 M., Xie, P., Shaw, M. D., Lewis, A. C., Mehra, A., Bannan, T. J., Worrall, S. D., Priestley, M.,
819 Bacak, A., Coe, H., Allan, J., Percival, C. J., Popoola, O. A. M., Jones, R. L., and Bloss, W. J.:
820 Intercomparison of nitrous acid (HONO) measurement techniques in a megacity (Beijing),
821 Atmos. Meas. Tech., 12, 6449-6463, https://doi.org/10.5194/amt-12-6449-2019, 2019.

822   de Jesus Madeiros, D., and Pimentel, A. S.: New insights in the atmospheric HONO formation:
823   new pathways for N_2O_4 isomerisaton and NO_2 dimerisation in the presence of water. , J. Phys.
824   Chem. A, 115, 6357-6365, https://doi.org/10.1021/jp1123585, 2011.

825   Dupart, Y., Fine, L., D'Anna, B., and George, C.: Heterogeneous uptake of NO_2 on Arizona
826   Test Dust under UV-A irradiation: an aerosol flow tube study, Aeolian Res., 15, 45-51,
827   https://doi.org/10.1016/j.aeolia.2013.10.001, 2014.

828   Fateley, W. G., Bent, H. A., and Crawford Jr, B.: Infrared spectra of the frozen oxides of
829   nitrogen, J. Chem. Phys., 31, 204-217, https://doi.org/10.1063/1.1730296, 1959.

830   Finlayson-Pitts, B. J., Wingen, L. M., Summer, A. L., Syomin, D., and Ramazan, K. A.: The
831   heterogeneous hydrolysis of NO_2 in laboratory systems in outdoor and indoor atmospheres: An
832   intergrated mechanism, Phys.Chem.Phys.Chem, 5, 223-242, https://doi.org/10.1039/b208564j,
833   2003.

834   Forney, D., Thompson, W. E., and Jacox, M. E.: The vibrational spectra of molecular ions
835   isolated in solid neon. XI. NO_2^+, NO_2^-, and NO_3^-, The Journal of Chemical Physics, 99, 7393-
836   7403, https://doi.org/10.1063/1.465720, 1993.

837   George, C., Strekowski, R. S., Kleffmann, J., Stemmler, K., and Ammann, M.: Photoenhanced
838   uptake of gaseous NO_2 on solid organic compounds: a photochemical source of HONO?,
839   Faraday Discuss., 130, https://doi.org/10.1039/b417888m, 2005.

840   George, I. J., Matthews, P. S. J., Whalley, L. K., Brooks, B., Goddard, A., Baeza-Romero, M.,
841   and Heard, D. E.: Measurements of uptake coefficients for heterogeneous loss of HO_2 onto
842   submicron inorganic salt aerosols., Phys. Chem. Chem. Phys., 15, 12829-12845,
843   https://doi.org/10.1039/c3cp51831k, 2013.

844   Ginoux, P., Chin, M., Tegen, I., Prospero, J. M., Holben, B., Dubovik, O., and Lin, S. J.:
845   Sources and distributions of dust aerosols simulated with the GOCART model, J. Geophys.
846   Res. Atmos., 106, 20255-20273, https://doi.org/10.1029/2000JD000053, 2001.

847   Givan, A., and Loewenschuss, A.: Fourier transform infrared and Raman studies on solid
848   nitrogen dioxide: Temperature cycling of ordered, disordered, and multicomponent layers, The
849   Journal of Chemical Physics, 90, 6135-6142, https://doi.org/10.1063/1.456379, 1989a.

850   Givan, A., and Loewenschuss, A.: On the intermolecularity or intramolecularity of nitrosonium
851   nitrate formation in thin films of nitrogen dioxide: A Fourier transform infrared study, The
852   Journal of chemical physics, 91, 5126-5127, https://doi.org/10.1063/1.457609, 1989b.

853   Givan, A., and Loewenschuss, A.: Fourier transform infrared study of amorphous N_2O_4 solid:
854   Destabilization with inert impurities, The Journal of chemical physics, 94, 7562-7563,
855   https://doi.org/10.1063/1.460192, 1991.

856   Goodman, A. L., Bernard, E. T., and Grassian, V. H.: Spectroscopic study of nitric acid and
857   water adsorption on oxide particles: enhanced nitric acid uptake kinetics in the presence of
858   adsorbed water, J. Phys. Chem. A, 105, 6443-6457, https://doi.org/10.1021/jp0037221, 2001.

859   Gustafsson, R. J., Orlov, A., Griffiths, P. T., Cox, R. A., and Lambert, R. M.: Reduction of
860   NO_2 to nitrous acid on illuminated titanium dioxide aerosol surfaces: implications for
861   photocatalysis and atmospheric chemistry, Chem. Commun., 37, 3936-3938,
862   https://doi.org/10.1039/b609005b, 2006.

863   Hanisch, F., and Crowley, J. N.: Ozone decomposition on Saharan dust: an experimental
864   investigation, Atmos. Chem. Phys., 3, 119-130, https://doi.org/10.5194/acp-3-119-2003, 2003.

865   Harrison, R. M., Peak, J. D., and Collins, G. M.: Tropospheric cycle of nitrous acid, J. Geophys.
866   Res. Atmos., 101, 14429-14439, https://doi.org/10.1029/96JD00341, 1996.

867   Heard, D. E.: Atmospheric field measurements of the hydroxyl radical using Laser-Induced
868   Fluorescence   spectroscopy,   Annu.   Rev.   Phys.   Chem.,   57,   191-216,
869   https://doi.org/10.1146/annurev.physchem.57.032905.104516, 2006.

870   Jeong, M.-G., Park, E. J., Seo, H. O., Kim, K.-D., Kim, Y. D., and Lim, D. C.: Humidity effect
871   on photocatalytic activity of TiO_2 and regeneration of deactivated photocatalysts, Appl. Surf.
872   Sci., 271, 164-170, https://doi.org/10.1016/j.apsusc.2013.01.155, 2013.

873   Kleffmann, J.: Daytime sources of nitrous acid (HONO) in the atmospheric boundary layer,
874   Chem. Phys. Chem., 8, 1137-1144, https://doi.org/10.1002/cphc.200700016, 2007.

875   Kurtenbach, R., Becker, K. H., Gomes, J. A. G., Kleffmann, J., Lörzer, J. C., Spittler, M.,
876   Wiesen, P., Ackermann, R., Geyer, A., and Platt, U.: Investigations of emissions and
877   heterogeneous formation of HONO in road traffic tunnel, Atmos. Environ., 35, 3385-3394,
878   https://doi.org/10.1016/S1352-2310(0)00138-8, 2001.

879   Lee, J. D., Whalley, L. K., Heard, D. E., Stone, D., Dunmore, R. E., Hamilton, J. F., Young,
880   D. E., Allan, J. D., Laufs, S., and Kleffmann, J.: Detailed budget analysis of HONO in central
881   London   reveals   a   missing   daytime   source,   Atmos.   Chem.   Phys.,   16,   2747-2764,
882   https://doi.org/10.5194/acp-16-2747-2016, 2016.

883   Levy, H.: Normal atmosphere: large radical and formaldehyde concentrations predicted,
884   Science, 173, 141-143, https://doi.org/10.1126/science.173.3992.141, 1971.

885   Li, S., Matthews, J., and Sinha, A.: Atmospheric hydroxyl radical production from
886   electronically excited NO_2 and H_2O, Science, 319, https://doi.org/10.1126/science.1151443,
887   2008.

888   Liao, W., Hecobian, A., Mastromarino, J., and Tan, D.: Development of a photo-
889   fragmentation/laser-induced fluorescence measurement of atmospheric nitrous acid,
890   Atmospheric Envrionment, 40, 17-26, https://doi.org/10.1016/j.atmosenv.2005.07.001, 2006.

891   Liu, W. G., and Goddard, W. A.: First-principle study of the role of interconversion between
892   NO_2, N_2O_4, cis-ONO-NO_2, and trans-ONO-NO_2 in chemical processes, J. Am. Chem. Soc.,
893   134, 12970-12978, https://doi.org/10.1021/ja300545e, 2012.

894   Lu, K., Fuchs, H., Hofzumahaus, A., Tan, Z., Wang, H., Zhang, L., Schmitt, S. H., Rohrer, F.,
895   Bohn, B., Broch, S., Dong, H., Gkatzelis, G. I., Hohaus, T., Holland, F., Li, X., Liu, Y., Liu,
896   Y., Ma, X., Novelli, A., Schlag, P., Shao, M., Wu, Y., Wu, Z., Zeng, L., Hu, M., Kiendler-
897   Scharr, A., Wahner, A., and Zhang, Y.: Fast Photochemistry in Wintertime Haze:
898   Consequences for Pollution Mitigation Strategies, Environ. Sci. Technol., 53, 10676-10684,
899   https://doi.org/10.1021/acs.est.9b02422, 2019.

900   Lu, X., Park, J., and Lin, M. C.: Gas phase reactions of HONO with NO_2, O_3 and HCl: Ab initio
901   and TST study, J. Phys. Chem. A, 104, 8730-8738, https://doi.org/10.1021/jp001610o, 2000.

902   Matthews, P. S. J., Baeza-Romero, M. T., Whalley, L. K., and Heard, D. E.: Uptake of HO_2
903   radicals onto Arizona test dust particles using an aerosol flow tube, Atmos. Chem. Phys., 14,
904   7397-7408, https://doi.org/10.5194/acp-14-7397-2014, 2014.

905   MCPA software Ltd.: Facsimile, 2020.

906   Michoud, V., Colomb, A., Borbon, A., Miet, K., Beekmann, M., Camredon, M., Aumont, B.,
907   Perrier, S., Zapf, P., Siour, G., Ait-Helal, W., Afif, C., Kukui, A., Furger, M., Dupont, J. C.,
908   Haeffelin, M., and Doussin, J. F.: Study of the unknown HONO daytime source at a European

909   suburban site during the MEGAPOLI summer and winter field campaigns, Atmos. Chem.
910   Phys., 14, 2805-2822, https://doi.org/10.5194/acp-14-2805-2014, 2014.

911   Moon, D. R., Taverna, G. S., Anduix-Canto, C., Ingham, T., Chipperfield, M. P., Seakins, P.
912   W., Baeza-Romero, M.-T., and Heard, D. E.: Heterogeneous reaction of HO_2 with airborne
913   TiO_2 particles and its implication for climate change mitigation strategies, Atmos. Chem. Phys.,
914   18, 327–338, https://doi.org/10.5194/acp-18-327-2018, 2018.

915   Moon, D. R., Ingham, T., Whalley, L. K., Seakins, P. W., Baeza-Romero, M. T., and Heard,
916   D. E.: Production of OH and HO_2 radicals from near-UV irradiated airborne TiO_2
917   nanoparticles, Phys.Chem.Phys.Chem, 21, 2325-2336, https://doi.org/10.1039/C8CP06889E,
918   2019.

919   Murdachaew, G., Varner, M. E., Philips, L. F., Finlayson-Pitts, B. J., and Gerber, R. B.:
920   Nitrogen dioxide at the air-water interface: trapping, adsorption, and solvation in the bulk and
921   at the surface, Phys. Chem. Chem. Phys., 15, 204-212, https://doi.org/10.1039/c2cp42810e,
922   2013.

923   Nakamura, I., Sugihara, S., and Takeuchi, K.: Mechanism for NO photooxidation over the
924   oxygen-deficient TiO_2 powder under visible light irradiation, Chem. Lett., 29, 1276-1277,
925   https://doi.org/10.1246/cl.2000.1276, 2000.

926   Ndour, M., D'Anna, B., George, C., Ka, O., Balkanski, Y., Kleffman, J., Stemmler, K., and
927   Ammann, M.: Photoenhanced uptake of NO_2 on mineral dust: Laboratory experiments and
928   model simulations, Geophys. Res. Lett., 35, L05812, https://doi.org/10.1029/2007GL032006,
929   2008.

930   Oswald, R., Behrendt, T., Ermel, M., Wu, D., Su, H., Cheng, Y., Breuninger, C., Moravek, A.,
931   Mougin, E., Delon, C., Loubet, B., Pommerening-Röser, A., Sörgel, M., Pöschl, U., Hoffmann,
932   T., Andeae, M. O., Meixner, F. X., and Trebs, I.: HONO emissions from soil bacteria as a
933   major source of atmospheric reactive nitrogen, Science, 341, 1233-1235,
934   https://doi.org/10.1126/science.1242266, 2013.

935   Pinnick, D., Agnew, S., and Swanson, B.: Fluid dinitrogen tetroxide at very high pressure and
936   high temperature: observation of the nitrite isomer, The Journal of Physical Chemistry, 96,
937   7092-7096, https://doi.org/10.1021/j100196a046, 1992.

938   Pitts, J. N., Sanhueza, E., Atkinson, R., Carter, W. P. L., Winer, A. M., Harris, G. W., and
939   Plum, C. N.: An investigation of the dark formation of nitrous acid in environmental chambers,
940   Int. J. Chem. Kinet., 16, 919-939, https://doi.org/10.1002/kin.550160712, 1984.

941   Platt, U., Perner, D., Harris, G. W., Winer, A. M., and Pitts, J. N.: Observations of nitrous acid
942   in an urban atmosphere by differential optical absorption, Nature, 285, 312-314,
943   https://doi.org/10.1038/285312a0, 1980.

944   Ramazan, K. A., Syomin, D., and Finlayson-Pitts, B. J.: The photochemical production of
945   HONO during the heterogeneous hydrolysis of NO2, Phys. Chem. Chem. Phys., 6, 3836-3843,
946   https://doi.org/10.1039/B402195A, 2004.

947   Ramazan, K. A., Wingen, L. M., Miller, Y., Chaban, G. M., Gerber, R. B., Xantheas, S. S., and
948   Finlayson-Pitts, B. J.: New experimental and theoretical approach to the heterogeneous
949   hydrolysis of NO2: key role of molecular nitric acid and its complexes, J. Phys. Chem. A, 110,
950   6886-6897, https://doi.org/10.1021/jp056426n, 2006.

951   Reed, C., Evans, M. J., Crilley, L. R., Bloss, W. J., Sherwen, T., Read, K. A., Lee, J. D., and
952   Carpenter, L. J.: Evidence for renoxification in the tropical marine boundary layer, Atmos.
953   Chem. Phys., 17, 4081-4092, https://doi.org/10.5194/acp-17-4081-2017, 2017.

954 Sakamaki, F., Hatakeyama, S., and Akimoto, H.: Formation of nitrous acid and nitric oxide in
955 the heterogeneous dark reaction of nitrogen dioxide and water vapor in a smog chamber, Int.
956 J. Chem. Kinet., 15, 1013-1029, https://doi.org/10.1002/kin.550151006, 1983.

957 Saliba, N., Moussa, S., and Tayyar, G.: Contribution of airborne dust particles to HONO
958 sources, Atmos. Chem. Phys. Discuss., 14, https://doi.org/10.5194/acpd-14-4827-2014, 2014.

959 Sander, S., Friedl, R., Barker, J., Golden, D., Kurylo, M., Wine, P., Abbatt, J., Burkholder, J.,
960 Kolb, C., and Moortgat, G.: Chemical kinetics and photochemical data for use in atmospheric
961 studies, evaluation number 14, JPL Publ., 02, 25, 2003.

962 Schleicher, N., Norra, S., Chai, F., Chen, Y., Wang, S., and Stüben, D.: Anthropogenic versus
963 geogenic contribution to total suspended atmospheric particulate matter and its variations
964 during a two-year sampling period in Beijing, China, J. Environ. Monit., 12, 434-441,
965 https://doi.org/10.1039/B914739J, 2010.

966 Seifert, N. A., Zaleski, D. P., Fehnel, R., Goswami, M., Pate, B. H., Lehmann, K. K., Leung,
967 H. O., Marshall, M. D., and Stanton, J. F.: The gas-phase structure of the asymmetric, trans-
968 dinitrogen tetroxide (N_2O_4), formed by dimerization of nitrogen dioxide (NO_2), from rotational
969 spectroscopy and ab initio quantum chemistry, The Journal of Chemical Physics, 146, 134305,
970 https://doi.org/10.1063/1.4979182, 2017.

971 Shan, J. H., Wategaonkar, S. J., and Vasudev, R.: Vibrational state dependence of the A state
972 lifetime of HONO, Chem. Phys. Lett., 158, 317-320, https://doi.org/10.1016/0009-
973 2614(89)87343-9, 1989.

974 Slater, E. J., Whalley, L. K., Woodward-Massey, R., Ye, C., Lee, J. D., Squires, F., Hopkins,
975 J. R., Dunmore, R. E., Shaw, M., Hamilton, J. F., Lewis, A. C., Crilley, L. R., Kramer, L.,
976 Bloss, W., Vu, T., Sun, Y., Xu, W., Yue, S., Ren, L., Acton, W. J. F., Hewitt, C. N., Wang, X.,
977 Fu, P., and Heard, D. E.: Elevated levels of OH observed in haze events during wintertime in
978 central Beijing, Atmos. Chem. Phys. Discuss., 2020, 1-43, https://doi.org/10.5194/acp-2020-
979 362, 2020.

980 Spataro, F., and Ianniello, A.: Sources of atmospheric nitrous acid: State of the science, current
981 research needs, and future prospects, J. Air Waste Manage. Assoc., 64, 1232-1250,
982 https://doi.org/10.1080/10962247.2014.952846, 2014.

983 Stemmler, K., Ndour, M., Elshorbany, Y., Kleffmann, J., D'Anna, B., George, C., Bohn, B.,
984 and Ammann, M.: Light induced conversion of nitrogen dioxide into nitrous acid on submicron
985 humic acid aerosol, Atmos. Chem. Phys., 7, 4237-4248, https://doi.org/10.5194/acp-7-4237-
986 2007, 2007.

987 Su, H., Cheng, Y., Oswald, R., Behrendt, T., Trebs, I., Meixner, F. C., Andreae, M. O., Cheng,
988 P., Zhang, Y., and Pöschl, U.: Soil nitrate as a source of atmospheric HONO and OH radicals,
989 Science, 333, 1616-1618, https://doi.org/10.1126/science.1207687, 2011.

990 Syomin, D. A., and Finlayson-Pitts, B. J.: HONO decomposition on borosilicate glass surfaces:
991 implications for environmental chamber studies and field experiments, Phys. Chem. Chem.
992 Phys., 5, 5236-5242, https://doi.org/10.1039/b309851f, 2003.

993 Takeuchi, M., Sakamoto, K., Martra, G., Coluccia, S., and Anpo, M.: Mechanism of
994 photoinduced superhydrophilicity on the TiO_2 photocatalyst surface, J. Phys. Chem. B, 109,
995 15422-15428, https://doi.org/10.1021/jp058075i, 2005.

996 Varner, M. E., Finlayson-Pitts, B. J., and Gerber, R. B.: Reaction of a charge-separated
997 $ONONO_2$ species with water in the formation of HONO: an MP2 molecular dynamics study,
998 Phys. Chem. Chem. Phys., 16, 4483-4487, https://doi.org/10.1039/c3cp55024a, 2014.

999   Wang, J., and Koel, B. E.: IRAS studies of NO_2, N_2O_3, and N_2O_4 adsorbed on Au (111) surfaces
1000 and reactions with coadsorbed H_2O, J. Phys. Chem. A, 102, 8573-8579,
1001 https://doi.org/10.1021/jp982061d, 1998.

1002 Wang, J., and Koel, B. E.: Reactions of N_2O_4 with ice at low temperatures on the Au (111)
1003 surface, Surf. Sci., 436, 15-28, https://doi.org/10.1016/S0039-6028(99)00457-4, 1999.

1004 Wexler, A. S., and Clegg, S. L.: Atmospheric aerosol models for systems including the ions
1005 H^+, NH_4^+, Na^+, SO_4^{2-}, NO_3^-, Cl^-, Br^-, and H_2O, J. Geophys. Res. Atmos., 107, ACH 14-11-
1006 ACH 14-14, https://doi.org/10.1029/2001JD000451, 2002.

1007 Whalley, L. K., Furneaux, K. L., Goddard, A., Lee, J. D., Mahajan, A., Oetjen, H., Read, K.
1008 A., Kaaden, N., Carpenter, L. J., Lewis, A. C., Plane, J. M. C., Saltzman, E. S., Wiedensohler,
1009 A., and Heard, D. E.: The chemistry of OH and HO_2 radicals in the boundary layer over the
1010 tropical Atlantic Ocean, Atmos. Chem. Phys., 10, 1555-1576, https://doi.org/10.5194/acp-10-
1011 1555-2010, 2010.

1012 Whalley, L. K., Stone, D., Dunmore, R., Hamilton, J., Hopkins, J. R., Lee, J. D., Lewis, A. C.,
1013 Williams, P., Kleffmann, J., Laufs, S., Woodward-Massey, R., and Heard, D. E.:
1014 Understanding in situ ozone production in the summertime through radical observations and
1015 modelling studies during the Clean air for London project (ClearfLo), Atmos. Chem. Phys., 18,
1016 2547-2571, https://doi.org/10.5194/acp-18-2547-2018, 2018.

1017 Whalley, L. K., Slater, E. J., Woodward-Massey, R., Ye, C., Lee, J. D., Squires, F., Hopkins,
1018 J. R., Dunmore, R. E., Shaw, M., Hamilton, J. F., Lewis, A. C., Mehra, A., Worrall, S. D.,
1019 Bacak, A., Bannan, T. J., Coe, H., Ouyang, B., Jones, R. L., Crilley, L. R., Kramer, L. J., Bloss,
1020 W. J., Vu, T., Kotthaus, S., Grimmond, S., Sun, Y., Xu, W., Yue, S., Ren, L., Acton, W. J. F.,
1021 Hewitt, C. N., Wang, X., Fu, P., and Heard, D. E.: Evaluating the sensitivity of radical
1022 chemistry and ozone formation to ambient VOCs and NOx in Beijing, Atmos. Chem. Phys.
1023 Discuss., 2020, 1-41, https:\\doi.org\10.5194/acp-2020-785, 2020.

1024 Winer, A. M., and Biermann, H. W.: Long pathlength differential optical absorption
1025 spectroscopy (DOAS) measurements of gaseous HONO, NO_2 and HCNO in the California
1026 South Coast Air Basin, Res. Chem. Intermed., 20, 423-445,
1027 https://doi.org/10.1163/156856794X00405, 1994.

1028 Wu, L., Li, X., and Ro, C.: Hygroscopic behavior of ammonium sulfate, ammonium nitrate,
1029 and their mixture particles, Asian J. Atmos. Environ., 13.3, 196-211,
1030 https://doi.org/10.5572/ajae.2019.13.3.196, 2019.

1031 Ye, C., Zhou, X., Pu, D., Stutz, J., Festa, J., Spolaor, M., Tsai, C., Cantrell, C., Mauldin, R. L.,
1032 Campos, T., Weinheimer, A., Hornbrook, R. S., Apel, E. C., Guenther, A., Kaser, L., Yuan,
1033 B., Karl, T., Haggerty, J., Hall, S., Ullmann, K., Smith, J. N., Ortega, J., and Knote, C.: Rapid
1034 cycling of reactive nitrogen in the marine boundary layer, Nature, 532, 489-491,
1035 https://doi.org/10.1038/nature17195, 2016.

1036 Ye, C., Heard, D. E., and Whalley, L. K.: Evaluation of novel routes for NO_x formation in
1037 remote regions. , Environmental Science Technology, 51, 7442-7449,
1038 https://doi.org/acs.est.6b06441, 2017a.

1039 Ye, C., Zhang, N., Gao, H., and Zhou, X.: Photolysis of particulate nitrate as a source of HONO
1040 and NO_x, Environ. Sci. Technol., 51, 6849-6856, https://doi.org/10.1021/acs.est.7b00387,
1041 2017b.

1042   Zhou, X., Gao, H., He, Y., Huang, G., Bertman, S. B., Civerolo, K., and Schwab, J.: Nitric acid
1043   photolysis on surfaces in low NO_x environments: Significant atmospheric implications,
1044   Geophys. Res. Lett., 30, 2217, https://doi.org/10.1029/2003GL018620, 2003.

1045

1046